

## The Consequences of Surface-Exchange Coefficient Uncertainty on an Otherwise Highly Predictable Major Hurricane

ROBERT G. NYSTROM<sup>a</sup> AND FALKO JUDT<sup>a</sup>

<sup>a</sup> National Center for Atmospheric Research, Boulder, Colorado

(Manuscript received 7 December 2021, in final form 16 March 2022)

**ABSTRACT:** In addition to initial conditions, uncertainty in model physics can also influence the practical predictability of tropical cyclones. In this study, the influence that various magnitudes of uncertainty in the surface exchange coefficients of momentum ( $C_d$ ) and enthalpy ( $C_k$ ) can have on an otherwise highly predictable major hurricane (Hurricane Patricia) is compared with that resulting from climatological environmental initial condition uncertainty and the intrinsic limit for this case. As the systematic uncertainty in  $C_d$  and  $C_k$  is reduced from 40% to 1%, the simulated uncertainty in the intensity and structure is substantially reduced and approaches the intrinsic limit when uncertainty is reduced to 1%. In addition, the forecasted intensity and structure uncertainty only becomes less than that resulting from climatological environmental initial condition uncertainty once the systematic uncertainty in  $C_d$  and  $C_k$  is reduced to ~10%, highlighting the strong influence of model error in limiting TC predictability. If  $C_d$  and  $C_k$  are perturbed stochastically, instead of systematically, it is shown that the influence on the simulated intensity and structure is negligible and nearly identical to the intrinsic limit, regardless of the magnitude of the stochastic  $C_d$  and  $C_k$  perturbations. While the magnitude of the stochastic  $C_d$  and  $C_k$  perturbations are comparable to the systematic perturbations, the stochastic perturbations are shown to not substantially perturb the time-integrated inner-core fluxes of momentum or enthalpy that predominantly determine simulated tropical cyclone intensity. Last, it is shown that the kinetic energy error growth behavior varies with the radius, azimuthal wavenumber, and ensemble design.

**SIGNIFICANCE STATEMENT:** The air-sea energy exchange beneath hurricanes is highly uncertain but strongly influences intensity. In this study, the influences of different magnitudes of surface-exchange coefficient uncertainty on the simulated intensity of an intense hurricane is compared with that resulting from environmental initial condition uncertainty and the intrinsic predictability limit. The main takeaway is that current surface-exchange coefficient uncertainties result in larger intensity uncertainty than environmental initial condition uncertainty, and substantial improvements in predictions are possible if current surface-exchange coefficient uncertainties are reduced. Furthermore, it is shown that randomly perturbing the surface-exchange coefficients at each point in space and time is not the best approach to account for the influences of this uncertain physical process on hurricane prediction because it has minimal influence on the simulated intensity.

**KEYWORDS:** Hurricanes/typhoons; Tropical cyclones; Air-sea interaction; Surface fluxes; Ensembles; Numerical weather prediction/forecasting; Model errors

### 1. Introduction

Tropical cyclones (TCs) are devastating natural disasters that are challenging to predict. TC intensity is a specifically difficult detail to predict in numerical models because of the importance in accurately representing coupled ocean-atmosphere processes (e.g., Sanford et al. 1987; Bender et al. 1993; Davis et al. 2008; Nystrom et al. 2020a) and the influence of both environmental conditions and the TC inner-core structure (e.g., Judt et al. 2015; Tao and Zhang 2015; Emanuel and Zhang 2016). In this study, we focus on the strong influences of uncertainty in the surface-exchange coefficients of momentum ( $C_d$ ) and enthalpy ( $C_k$ ) on the predictability of an intense TC.

While the surface-exchange coefficients are only one aspect of model physics that can influence the predictability of TCs, their influence on simulated TCs is well established from both a theoretical dynamics prospective (e.g., Ooyama 1969; Rotunno

and Emanuel 1987; Emanuel 2012; Wang et al. 2021) and in practical applications simulating real TCs (e.g., Green and Zhang 2013; Torn 2016; Nystrom and Zhang 2019). The maximum potential intensity (MPI) of tropical cyclones is believed to be determined by a balance between surface entropy fluxes and frictional dissipation (Emanuel 1997). More specifically, the MPI can be derived by equating the entropy gained from the ocean to the momentum lost through surface friction as

$$\int_{r_m}^{r_0} \rho \epsilon T_s C_k V(s_o^* - s_b) r dr = \int_{r_m}^{r_0} \rho C_d V^3 r dr, \quad (1)$$

where  $r_m$  is the radius of maximum wind speed (RMW),  $r_0$  is an outer radius,  $\rho$  is the boundary layer air density,  $T_s$  is the sea surface temperature,  $\epsilon$  is the thermodynamic efficiency [ $\epsilon = (T_s - T_o)/T_s$ ; where  $T_o$  is the outflow temperature],  $V$  is the surface wind speed,  $s_o^*$  is the saturation entropy with respect to the sea surface,  $s_b$  is the entropy of the boundary layer air, and  $r$  is the radius. If it is further assumed that the largest contributions from both the surface entropy flux and frictional dissipation take place at the RMW, where the wind

Corresponding author: Robert G. Nystrom, nystrom@ucar.edu

speed is maximized, the maximum potential wind speed ( $V_m$ ) can be estimated as

$$V_m^2 = \frac{C_k}{C_d} \epsilon T_s (s_o^* - s_b) |_m \quad (2)$$

Therefore, the MPI can be modified in nature or numerical models by changing the air-sea thermodynamic disequilibrium, the thermodynamic efficiency, or the ratio of the surface exchange coefficients ( $C_k/C_d$ ).

While the simulated intensity of TCs is well known to be sensitive to the model representations of  $C_d$  and  $C_k$ , the wind speed dependent representations of these variables are highly uncertain, especially at high wind speeds (Sroka and Emanuel 2021). It is estimated that the current uncertainty in  $C_d$  for wind speeds greater than hurricane force is at least 40%–50% (Bell et al. 2012; Richter et al. 2016) and as large as 200% for  $C_k$  (Richter et al. 2016). Considerable uncertainty remains in  $C_d$  and  $C_k$  at high wind speeds because of limited observations and substantial disagreements between studies attempting to estimate  $C_d$  and  $C_k$  from both the atmosphere and ocean sides (e.g., Jarosz et al. 2007; Komori et al. 2018; Hsu et al. 2019; Currie and Haus 2020; Troitskaya et al. 2020; Sroka and Emanuel 2021). Furthermore, Richter et al. (2021) demonstrated that the commonly used flux-profile may result in low biased  $C_d$  estimates near the eyewall, because of limited sampling, and we may therefore have pushed this approach toward estimating  $C_d$  beyond its limit. As a result,  $C_d$  and  $C_k$  uncertainty remains one major source of uncertainty in numerical models limiting our ability to improve TC intensity prediction.

Much of the previous research on TC predictability has focused on either the role of environmental conditions, such as vertical wind shear, or inner-core dynamics in limiting TC predictability (e.g., Van Sang et al. 2008; Zhang and Sippel 2009; Torn and Cook 2013; Zhang and Tao 2013; Judt et al. 2015; Torn 2016; Emanuel and Zhang 2017; Nystrom et al. 2018). One challenge in quantifying the predictability of TCs is that it appears to be a function of environmental conditions and varies throughout the storm life cycle, being most limited near genesis and rapid intensification onset. Despite these challenges, recent studies have suggested a significant gap between our prediction abilities with currently available procedures (practical predictability) and the best possible predictions with a nearly perfect model and nearly perfect knowledge of the current atmospheric state (intrinsic predictability limit) (e.g., Emanuel and Zhang 2016).

Building on the predictability work of Lorenz (1969) and Rotunno and Snyder (2008), Judt et al. (2015) analyzed the kinetic energy (KE) error spectra of a real Atlantic hurricane (Earl 2010) and demonstrated that errors rapidly grew and saturated for the small scales while the azimuthal wavenumbers 0 and 1 remained predictable through at least 168 h. In addition, the error growth and the magnitude of ensemble variance was found to increase with the spatial scale of the stochastic perturbations. One key difference from the classical turbulence perspective, however, is that predictability should be evaluated at statistical equilibrium, which

TCs in nature seldom—if ever—reach. With that said, Brown and Hakim (2013) analyzed an idealized 100-day simulation at statistical equilibrium and used inverse modeling to suggest that the intrinsic predictability limit of TCs is ~2 days. Conversely, Kieu and Moon (2016) suggested that the MPI acts as an attractor and therefore TC intensity is predictable within 8–10 m s<sup>-1</sup> near 5 days under favorable environmental conditions.

The present study explores the influences of model error on TC predictability. By perturbing  $C_d$  and  $C_k$ , the influences of uncertainty in the model attractor (MPI) on TC predictability is also explored. The primary objectives of this study are to 1) quantify the influences of  $C_d$  and  $C_k$  uncertainty on the predictability of a real TC, 2) compare the influences of  $C_d$  and  $C_k$  uncertainty with uncertainty resulting from environmental initial condition (IC) uncertainty and the intrinsic limit, and 3) demonstrate the differences between systematically and stochastically perturbing  $C_d$  and  $C_k$ . Section 2 provides a basic overview of the ensemble designs and model set up, section 3 presents multiple metrics of TC predictability and error growth, and section 4 has some concluding discussion.

## 2. Modeling methodology and ensemble design

To assess the influences of uncertainty in the model representations of  $C_d$  and  $C_k$  on TC predictability, we conducted a series of ensemble forecasts of Hurricane Patricia (2015). While only a single case, this hurricane was chosen for two main reasons. First, Patricia has been previously shown to have high intrinsic predictability (e.g., Fox and Judd 2018) but yet real-time predictions were very poor (e.g., Kimberlain et al. 2016; Rogers et al. 2017). Second, uncertainty in the surface-exchange coefficients was suggested to be at least one factor limiting the practical predictability (Nystrom and Zhang 2019).

### a. Modeling framework overview

All model simulations in this study were conducted using the Weather Research and Forecasting (WRF) Model, version 3.9.1 (Skamarock et al. 2008). The WRF Model is configured with four nested domains, each with two-way feedbacks, horizontal grid spacing of 29, 9, 3, and 1 km, respectively ( $378 \times 243$ ,  $297 \times 297$ ,  $297 \times 297$ , and  $297 \times 297$  grid points, respectively) and the three innermost domains are vortex following. Model physics options excluding the surface layer physics, which will be perturbed in this study, are identical to those of Nystrom et al. (2021). All simulations are uncoupled (atmosphere only) with identical sea surface temperatures (SSTs) and, unless otherwise perturbed, initial atmospheric conditions are taken to be those from the 2100 UTC 21 October EnKF analysis mean presented in Nystrom and Zhang (2019), which assimilated all available conventional observations and airborne tail Doppler radar radial velocity observations (Weng and Zhang 2012, 2016). The boundary conditions for all ensembles are also taken from the cycling data assimilation experiment presented in Nystrom and Zhang (2019), originating initially from the operational Global Forecast System (GFS). All simulations are initialized from 2100 UTC 21 October and

run until 1200 UTC 24 October, approximately 12 h after landfall.

In WRF the surface fluxes of sensible heat (SH), latent heat (LH), and momentum ( $\tau$ ) are calculated as

$$\text{SH} = -\rho c_p C_H V_{10} \Delta\theta, \quad (3)$$

$$\text{LH} = -\rho L_v C_q V_{10} \Delta q, \quad \text{and} \quad (4)$$

$$\tau = -\rho C_d V_{10}^2, \quad (5)$$

where  $\rho$  is the density of air,  $c_p$  is the specific heat capacity of air,  $C_H$  is the bulk exchange coefficient for sensible heat,  $V_{10}$  is the total 10-m wind speed,  $\Delta\theta$  is the potential temperature difference between the sea surface and the boundary layer air at 10 m,  $L_v$  is the enthalpy of vaporization,  $C_q$  is the bulk exchange coefficient for latent heat,  $\Delta q$  is the water vapor mixing ratio disequilibrium between the sea surface and the boundary layer air at 10 m, and  $C_d$  is bulk drag coefficient.

### b. Ensemble configurations

In this study we present nine ensemble sets of 20 members each (180 simulations in total). The first group of ensemble sets explores the influences of varying magnitudes (40%, 30%, 20%, 10%, or 1%) of systematic uncertainty in the surface-exchange coefficients ( $C_d$  and  $C_k$ ) on TC predictability. These ensembles are generated by systematically perturbing three parameters ( $\alpha$ ,  $V_c$ ,  $\beta$ ) which systematically modify  $C_d$  and  $C_k$ . More specifically,  $C_d$  is modified directly by  $\alpha$  and  $V_c$  as

$$C_d = \alpha \times \max[5, -0.014 \times \min(V_c, V_{10})^2 + 1.033 \times \min(V_c, V_{10}) + 4.895] \times 10^{-4}, \quad (6)$$

where  $\alpha$  is a multiplicative factor on  $C_d$  at all wind speeds,  $V_c$  acts to saturate  $C_d$  above a given wind speed threshold, and  $V_{10}$  is the total 10 m wind speed. Additionally,  $C_h$  (heat exchange coefficient) and  $C_q$  (moisture exchange coefficient) are directly perturbed by  $\beta$ , and indirectly perturbed by  $\alpha$  and  $V_c$  through  $C_d$ , as

$$C_h = \beta \times \frac{C_d}{1 + C_d^{1/2} \times (7.3 R_e^{1/4} P_r^{1/2} - 5)}, \quad (7)$$

and

$$C_q = \beta \times \frac{C_d}{1 + C_d^{1/2} \times (7.3 R_e^{1/4} S_c^{1/2} - 5)}, \quad (8)$$

where  $\beta$  is a multiplicative factor on  $C_h$  and  $C_q$  at all wind speeds,  $R_e$  is the roughness Reynolds number ( $R_e = u^* z_0 / v$ , where  $u^*$  is the friction velocity,  $z_0$  is the surface roughness length and  $v$  is the kinematic viscosity of air),  $P_r$  is the Prandtl number, and  $S_c$  is the Schmidt number (as in Nystrom et al. 2020b, 2021). To create the ensembles with varying magnitudes of uncertainty,  $\alpha$ ,  $V_c$ , and  $\beta$  are each perturbed by randomly sampling from a Gaussian distribution with a mean of  $\alpha = 1.0$ ,  $V_c = 52.0$ , and  $\beta = 1.0$  and standard deviation ( $\sigma$ ) of  $\sigma_\alpha = 0.4$ ,

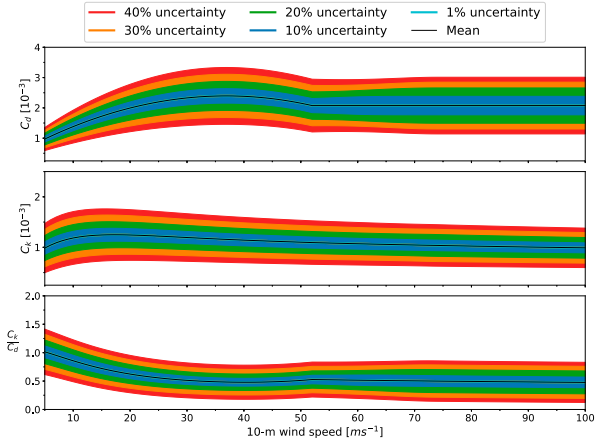


FIG. 1. Profiles of (top)  $C_d$ , (middle)  $C_k$ , and (bottom)  $C_k/C_d$  as a function of wind speed with various magnitudes of uncertainty.

$0.3$ ,  $0.2$ ,  $0.1$ , and  $0.01$ ,  $\sigma_{V_c} = 20.8$ ,  $15.6$ ,  $10.4$ ,  $5.2$ , and  $0.52$ ,  $\sigma_\beta = 0.4$ ,  $0.3$ ,  $0.2$ ,  $0.1$ , and  $0.01$ , for the 40%, 30%, 20%, 10%, and 1% uncertainty ensembles, respectively. The approximate range of uncertainty in  $C_d$  and  $C_k$  resulting from this random sampling is shown in Fig. 1.

To highlight the difference between stochastically and systematically perturbing  $C_d$  and  $C_k$ , two additional ensemble sets (Stochastic and 2xStochastic) stochastically perturb  $C_d$ ,  $C_h$ , and  $C_q$  by randomly sampling a normal distribution with mean 0 and  $\sigma_{C_d} = 0.5 \times 10^{-3}$  or  $1.0 \times 10^{-3}$  and  $\sigma_{C_k} = 0.2 \times 10^{-3}$  or  $0.4 \times 10^{-3}$  (as in Torn 2016 for Stochastic and double the magnitude for 2xStochastic) for each grid cell each time step that the WRF surface layer code is called. The approximate range of uncertainty in  $C_d$  and  $C_k$  resulting from these stochastic perturbations are shown in Fig. 2. It is important to note that this approach (Stochastic and 2xStochastic) differs from the systematic uncertainty (Fig. 1) in that perturbations are spatially and temporally uncorrelated. Therefore, the time-integrated domain-averaged  $C_d$  and  $C_k$  will be approximately the same for all stochastic ensemble members.

Last, two additional ensemble sets with either climatological environmental perturbations (CV3) or very small low-level water vapor mixing ratio perturbations (Intrinsic),  $\pm 0.5 \text{ g kg}^{-1}$  as in Van Sang et al. (2008) and Zhang and Tao (2013), are presented as a reference for comparison to the influence of environmental IC uncertainty and the intrinsic predictability limit, respectively. By adding only very small low-level water vapor mixing ratio perturbations we can interpret this ensemble as sampling the intrinsic predictability limit for this case because we have nearly a perfect knowledge of the initial state of the atmosphere.

### c. Tropical cyclone scale-dependent predictability

To quantify the scale-dependent error growth, the ensemble mean kinetic energy ( $\bar{KE}$ ) and the ensemble mean KE error ( $\bar{E}$ ) are calculated from the 10 m wind speed, as in Judt et al. (2015). The Fourier-decomposed KE is calculated in the

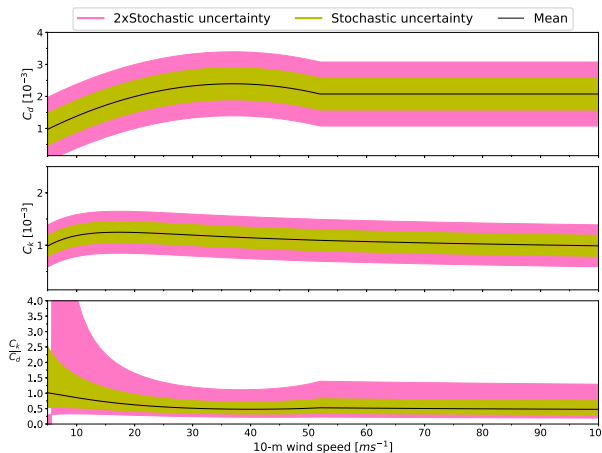


FIG. 2. Profiles of (top)  $C_d$ , (middle)  $C_k$ , and (bottom)  $C_k/C_d$  as a function of wind speed with various magnitudes of stochastic perturbations.

azimuthal direction from the 10-m wind field in polar coordinates. One consequence of using this methodology is that the spatial scale of all azimuthal wavenumbers varies (increases) with radius. Despite this, wavenumber 0 can be interpreted as representing the axisymmetric TC structure, wavenumber 1 the asymmetric TC structure, wavenumbers 2–5 the TC rainbands, and wavenumbers  $\geq 6$  as convective scale structures. The storm-scale  $\overline{KE}$  is calculated by performing a 1-day azimuthal Fourier-decomposition of the ensemble mean 10-m wind field ( $\bar{V}$ ) in cylindrical coordinates and averaging the power spectra within some outer radius ( $r_0$ ;  $r_0 = 150$  km here). Mathematically, the area-averaged  $\overline{KE}$  per wavenumber ( $k$ ) is calculated as

$$\overline{KE}(k) = \frac{1}{2} \int_0^{r_0} |\bar{V}(k, r)|^2 r dr. \quad (9)$$

Similarly, the storm-scale  $\overline{E}$  is calculated by performing a 1-day azimuthal Fourier-decomposition on the ensemble perturbation 10-m wind field ( $V'$ ; where  $V' = V - \bar{V}$ ) and averaged across all ensemble members. Mathematically, the area-averaged  $\overline{E}$  is calculated as

$$\overline{E}(k) = \sum_{m=1}^{20} \frac{1}{2} \int_0^{r_0} |V'_m(k, r)|^2 r dr, \quad (10)$$

where  $V'_m$  is the ensemble member perturbation wind field, sometimes alternatively referred to as the error field.

By comparing the mean KE ( $\overline{KE}$ ) with the mean error ( $\overline{E}$ ) the scale dependent error growth can be examined. In addition, the errors are considered saturated—or predictability is lost—for that scale (wavenumber) in statistical equilibrium when

$$\overline{E} = 2\overline{KE} \quad (11)$$

(Lorenz 1969). Physically this occurs when the forecast is wrong about the pattern with variance  $\overline{E}$  and is completely

out of phase with  $\overline{KE}$  for a given wavenumber. When considering a vortex, like a TC, this will never occur for wavenumber 0 so long as there is a vortex present (e.g., Judt et al. 2015). This suggests that the storm-scale axisymmetric TC structure is always predictable.

To partially examine the sensitivity of the error saturation to the area over which  $\overline{KE}$  and  $\overline{E}$  are calculated, as well as to emphasize the predictability of the eyewall itself, the eyewall mean kinetic energy ( $\overline{KE}_m$ ) and mean kinetic error energy ( $\overline{E}_m$ ) are also calculated within a narrow ring centered on the ensemble mean radius of maximum winds ( $\bar{r}_m$ ;  $\pm 4$  km) as

$$\overline{KE}_m(k) = \frac{1}{2} \int_{\bar{r}_m - 4\text{km}}^{\bar{r}_m + 4\text{km}} |\bar{V}(k, r)|^2 r dr \quad (12)$$

and

$$\overline{E}_m(k) = \sum_{m=1}^{20} \frac{1}{2} \int_{\bar{r}_m - 4\text{km}}^{\bar{r}_m + 4\text{km}} |V'_m(k, r)|^2 r dr, \quad (13)$$

respectively. By averaging over only the eyewall, the results should be more representative of only TC intensity and therefore more similar to that discussed in Brown and Hakim (2013).

### 3. Results and discussion

#### a. Predictability of TC intensity metrics

Overall, the ensemble mean maximum 10-m wind speed ( $V_{\max}$ ) and minimum central pressure ( $P_{\min}$ ) of each ensemble is nearly identical at all forecast times (Fig. 3). Furthermore, there is good confidence in a rapid intensification into a category-5 major hurricane in all ensembles. The ensemble mean  $V_{\max} \pm 1\sigma$  is greater than category four intensity, in all ensembles by 42 h.

On the other hand, the uncertainty in  $V_{\max}$  or  $P_{\min}$  clearly varies considerably between the ensembles (Figs. 3 and 4). Before landfall (ranging from 48 to 63 h), the largest uncertainty in  $V_{\max}$  or  $P_{\min}$  among the ensembles is found in the 40% systematic  $C_d$  and  $C_k$  uncertainty ensemble. With 40% systematic uncertainty in  $C_d$  and  $C_k$  the ensemble standard deviation near the time of peak intensity (42 h) for  $V_{\max}$  ( $\sigma_{V_{\max}}$ ) and  $P_{\min}$  ( $\sigma_{P_{\min}}$ ) is  $16 \text{ m s}^{-1}$  and  $34 \text{ hPa}$ , respectively. When the systematic uncertainty in  $C_d$  and  $C_k$  is reduced to 30% or 20%, the ensemble  $\sigma_{V_{\max}}$  and  $\sigma_{P_{\min}}$  is further reduced, relative to 40% systematic uncertainty. It is also noteworthy that uncertainty in  $P_{\min}$  is reduced when systematic  $C_d$  and  $C_k$  uncertainty is reduced from 30% to 20% but  $V_{\max}$  uncertainty is not (Fig. 4). This apparent difference in uncertainty reduction in  $V_{\max}$  and  $P_{\min}$  is likely related to the relative storm-scale nature of  $P_{\min}$  in comparison to the smaller scale—and thereby noisy—nature of  $V_{\max}$ . Continuing to reduce the systematic uncertainty in  $C_d$  and  $C_k$  to 10% or 1% further reduces the ensemble  $\sigma_{V_{\max}}$  and  $\sigma_{P_{\min}}$  (Fig. 4). Overall, reducing the systematic uncertainty in  $C_d$  and  $C_k$  from current levels ( $\sim 40\%$ ) substantially reduces the uncertainty in the pointwise metrics of TC intensity.

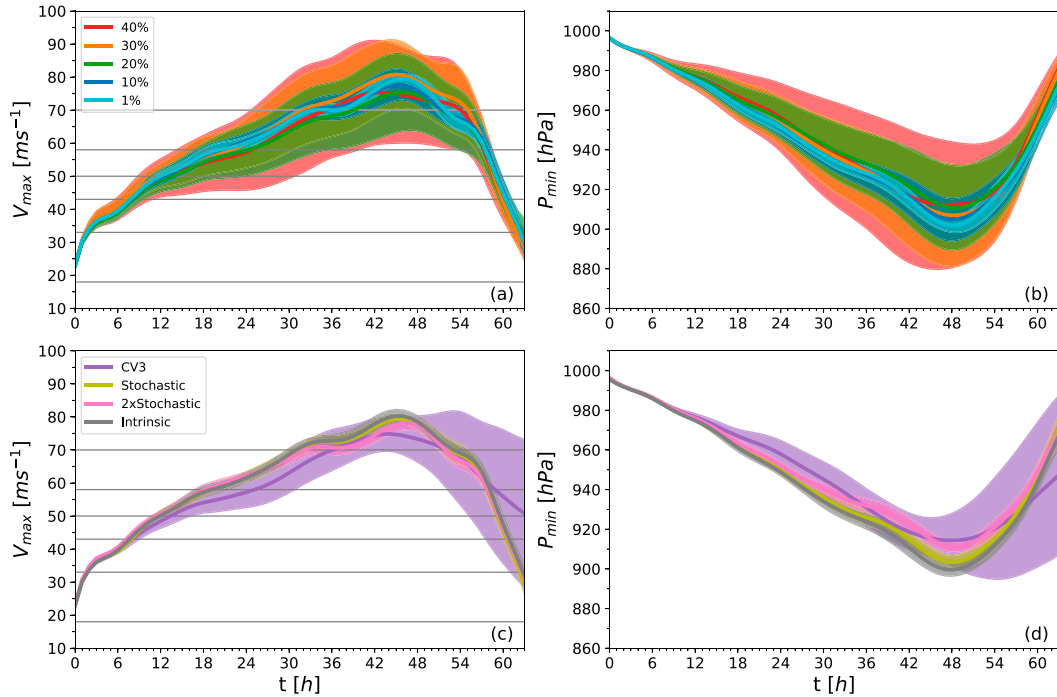


FIG. 3. Ensemble mean and standard deviation (shaded) of (a),(c) maximum 10-m wind speed and (b),(d) minimum surface pressure. Thin gray horizontal lines in (a) and (c) denote the wind speed thresholds for a tropical storm and category 1–5 hurricane on the Saffir–Simpson scale.

The uncertainty reduction in pointwise intensity metrics is nonlinear (Fig. 4). For example,  $\sigma_{V_{max}}$  and  $\sigma_{P_{min}}$  at 36 h are notably reduced when going from 40% to 30% systematic  $C_d$  and  $C_k$  uncertainty, but  $\sigma_{P_{min}}$  is only minimally and  $\sigma_{V_{max}}$  is not reduced when going from 30% to 20% systematic  $C_d$  and  $C_k$  uncertainty. Further reducing systematic  $C_d$  and  $C_k$  uncertainty from 20% to 10% again results in notably reduction of  $\sigma_{V_{max}}$  and  $\sigma_{P_{min}}$ , however. In other words, the reduction in simulated intensity uncertainty does not decrease at a constant rate with the reduction in  $C_d$  and  $C_k$  uncertainty.

When environmental perturbations alone are considered (CV3), the maximum simulated  $\sigma_{V_{max}}$  and  $\sigma_{P_{min}}$  over the first 45 h (prior to land interactions) are  $6 m s^{-1}$  and  $10 hPa$ , respectively (Fig. 4). After  $\sim 45$  h,  $\sigma_{V_{max}}$  and  $\sigma_{P_{min}}$  rapidly increase in CV3 because of uncertainties in landfall timing (landfall in

CV3 ranges from 48 h to never occurring during the simulation). In comparison with the influences of environmental IC uncertainties (CV3),  $\sigma_{V_{max}}$  and  $\sigma_{P_{min}}$  only become less than CV3 when systematic uncertainties in  $C_d$  and  $C_k$  are reduced to  $\sim 10\%$ . This suggests that uncertainties in  $C_d$  and  $C_k$  need to be reduced to  $\sim 10\%$  to be less limiting than current environmental IC uncertainty, at least when environmental conditions are very favorable for intensification as is the case here. In other words, reducing systematic  $C_d$  and  $C_k$  to  $\sim 10\%$  is critical to reduce intensity forecast uncertainty for this case. In addition, when  $C_d$  and  $C_k$  uncertainty is reduced to 1%,  $\sigma_{V_{max}}$  and  $\sigma_{P_{min}}$  become comparable to the intrinsic limit, suggesting there is no benefit to further reducing the uncertainties in  $C_d$  and  $C_k$  to 1% or beyond. The maximum  $\sigma_{V_{max}}$  and  $\sigma_{P_{min}}$  over the first 24 h in Intrinsic are  $2 m s^{-1}$  and  $5 hPa$ , respectively. This small

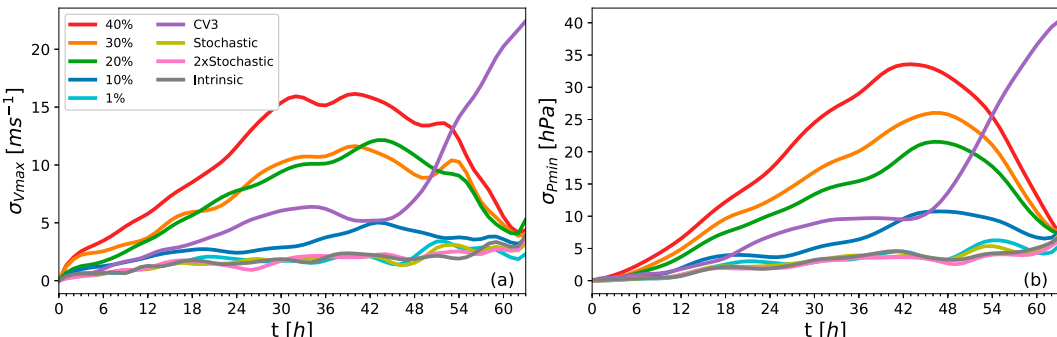


FIG. 4. Ensemble standard deviations for (left) maximum 10 m wind speed and (right) minimum surface pressure.

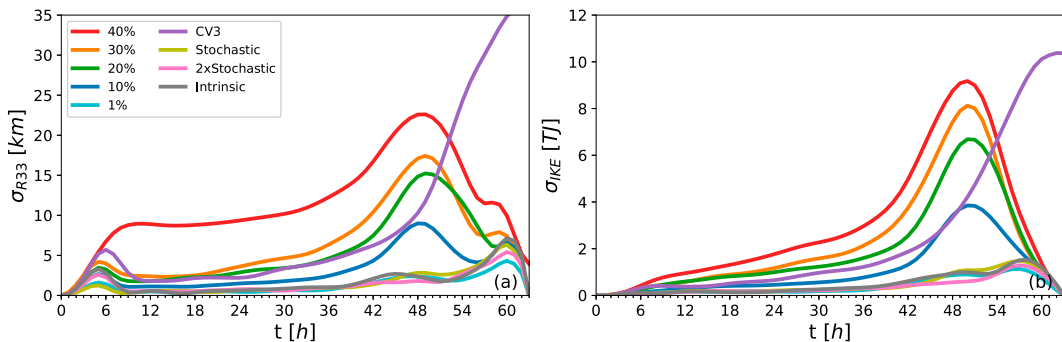


FIG. 5. Ensemble standard deviations for (left) radius of hurricane-force wind speed and (right) IKE.

intrinsic uncertainty in  $V_{\max}$  and  $P_{\min}$  is further indicative that the intensity of Patricia was highly predictable, at least at this forecast initialization time, consistent with Fox and Judt (2018) and Qin and Zhang (2018).

When  $C_d$  and  $C_k$  are perturbed stochastically (Stochastic and 2xStochastic)  $\sigma_{V_{\max}}$  and  $\sigma_{P_{\min}}$  are always minimal (maximum of  $2 \text{ m s}^{-1}$  and  $4 \text{ hPa}$ ), regardless of the magnitude of the stochastic perturbations (Figs. 3 and 4). Furthermore, even though the magnitude of the  $C_d$  and  $C_k$  perturbations are substantially larger than with 1% systematic uncertainty, the resulting forecast uncertainties in  $V_{\max}$  and  $P_{\min}$  are similar between 1% systematic, Stochastic, 2xStochastic, and Intrinsic. This result strongly suggests that stochastically perturbing  $C_d$  and  $C_k$  is not an appropriate approach to capture the impacts of their uncertainties on TC intensity prediction in numerical models, at least when perturbed randomly at each grid point in space and time.

#### b. TC structure predictability

In addition to pointwise metrics of TC intensity, TC structure is also sensitive to the magnitude of systematic uncertainty in  $C_d$  and  $C_k$ . Like  $V_{\max}$  and  $P_{\min}$ , the uncertainty in the radial extent of hurricane force winds uncertainty (R33;  $\sigma_{R33}$ ) decreases as the systematic uncertainty in  $C_d$  and  $C_k$  decreases (Fig. 5a). More specifically, as the systematic uncertainty in  $C_d$  and  $C_k$  is reduced from 40% to 30%, 20%, 10%, or 1%,  $\sigma_{R33}$  at 42 h is reduced from 17 to 10, 7, 4, and 2 km, respectively. This corresponds to a 41%, 59%, 76%, and 88% reduction in  $\sigma_{R33}$  at 42 h relative to 40% systematic  $C_d$  and  $C_k$  uncertainty for 30%, 20%, 10%, and 1%, respectively. It is also noteworthy that for the first  $\sim 24$  h  $\sigma_{R33}$  is similar for all ensembles except 40%  $C_d$  and  $C_k$  systematic uncertainty. This suggests that even modest reductions in current  $C_d$  and  $C_k$  can substantially reduce uncertainty in the radial extent of hurricane-force winds at short lead times. Furthermore, the large gap in  $\sigma_{R33}$  between 40% and 30% systematic  $C_d$  and  $C_k$  uncertainty suggests the presence of a key threshold in the predictability of the radial extent of hurricane force winds, namely that R33 is very sensitive to large systematic  $C_d$  and  $C_k$  but resilient to smaller  $C_d$  and  $C_k$  perturbations.

When  $C_d$  and  $C_k$  are perturbed stochastically  $\sigma_{R33}$  is also minimal ( $\sim 2$  km at 42 h; Fig. 5a), regardless of the magnitude of the stochastic perturbations. In addition,  $\sigma_{R33}$  with

stochastic  $C_d$  and  $C_k$  is always like Intrinsic, further highlighting that stochastically perturbing  $C_d$  and  $C_k$  has little influence on TC structure. Also, like  $V_{\max}$  and  $P_{\min}$ ,  $\sigma_{R33}$  in CV3 is nearly always less than 20%  $C_d$  and  $C_k$  systematic uncertainty, except for brief period near 6 h and near/after landfall. Therefore, reducing systematic  $C_d$  and  $C_k$  uncertainty to  $\sim 10\%$  appears necessary for large-scale environmental condition uncertainty to become as influential as systematic  $C_d$  and  $C_k$  uncertainty in modulating TC structure.

In addition to R33, the standard deviation of integrated kinetic energy (IKE;  $\sigma_{IKE}$ ) for hurricane force winds—an indicator of the overall destructiveness of a TC (Powell and Reinhold 2007)—consistently decreases from 5 to 0.5 TJ at 42 h as the systematic uncertainty in  $C_d$  and  $C_k$  is reduced from 40% to 1% (Fig. 5b). Also, like R33,  $\sigma_{IKE}$  only becomes less than CV3 when the systematic uncertainty in  $C_d$  and  $C_k$  is reduced to 10%. In addition, stochastically perturbing  $C_d$  and  $C_k$  has minimal influence on  $\sigma_{IKE}$  and is like Intrinsic, consistent with R33 and the pointwise intensity metrics. Other metrics of TC structure, such as the RMW or the radial extent of tropical storm force winds (R17), yield similar results (not shown).

In addition to differences in TC size, visual differences in the range of simulated convective structures are also apparent between the ensembles. As the systematic uncertainty in  $C_d$  and  $C_k$  is reduced from 40% to 10%, the uncertainty in the simulated convective structure is substantially reduced (Fig. 6). With 40% systematic  $C_d$  and  $C_k$  uncertainty there is large variability in the size of the TC eye, the spatial coverage of convection, and the eyewall is even partially open in some ensemble members. As the systematic uncertainty in  $C_d$  and  $C_k$  is reduced to 30%, 20%, or 10% the eye size and the spatial coverage of convection exhibits less variation within the ensemble, especially when the systematic  $C_d$  and  $C_k$  uncertainty is reduced to 10%. When the systematic  $C_d$  and  $C_k$  uncertainty is reduced to 10%, all ensemble members clearly simulate an intense hurricane with similar size and overall convective structures. Only small differences in the intensity and location of individual convective cells are still visible with 10% systematic  $C_d$  and  $C_k$  uncertainty.

Taking a closer look at the radial variability of the azimuthally averaged 10-m tangential wind ( $V_t$ ) field, the maximum standard deviation is found radially inward of the azimuthal mean radius

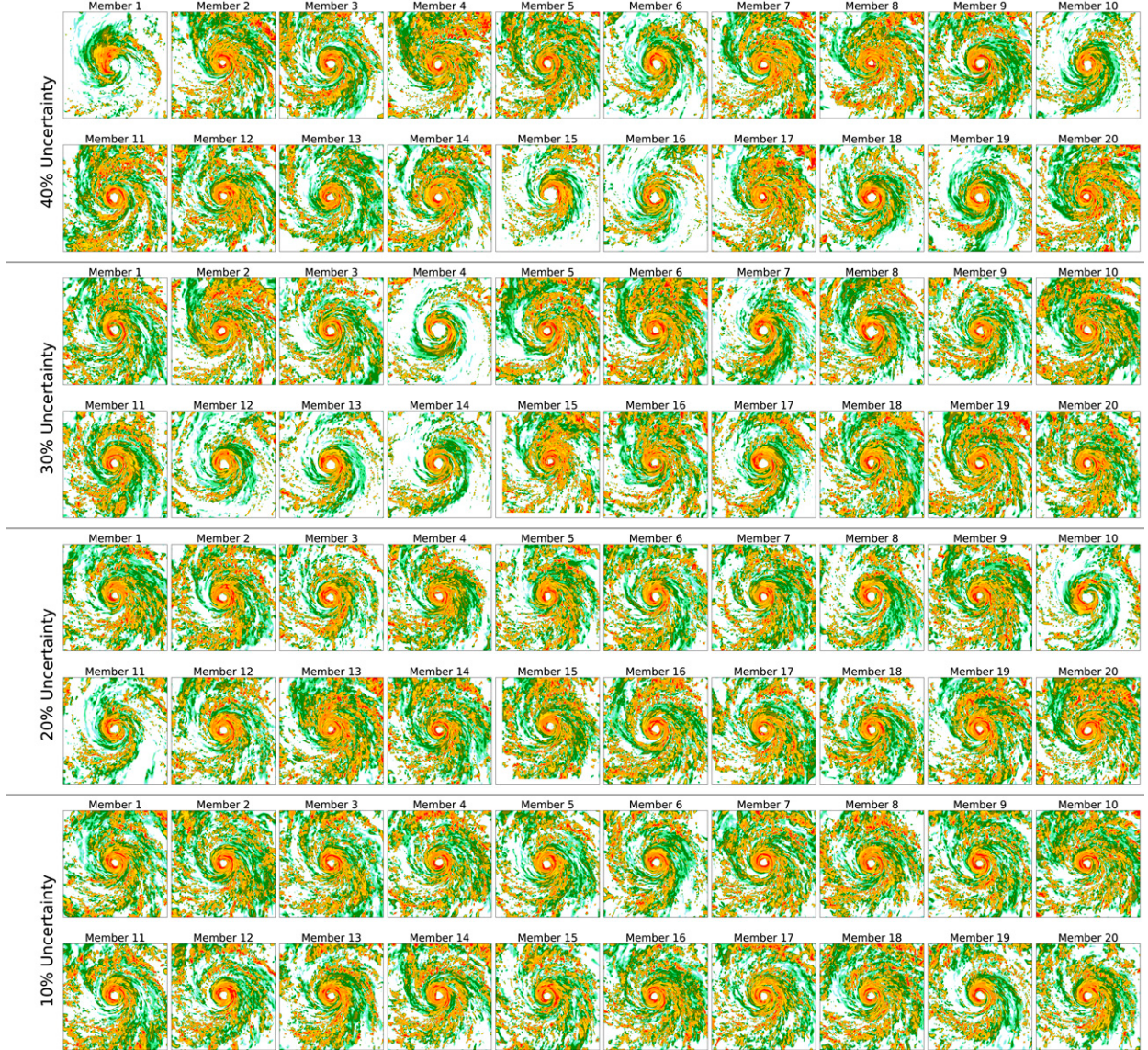


FIG. 6. Ensemble postage stamps of reflectivity at 1 km for (top two rows) 40%, (second two rows) 30%, (third two rows) 20%, and (bottom two rows) 10% systematic  $C_d$  and  $C_k$  uncertainty.

of maximum winds for all ensembles (Fig. 7). The maximum standard deviation for  $V_t$  ( $\sigma_{V_t}$ ) being found radially inward of the RMW is primarily the result of uncertainty in the location of the RMW and the sharp gradient in  $V_t$  radially inward of the RMW. As with the intensity and structure metrics,  $\sigma_{V_t}$  is reduced as the systematic uncertainty in  $C_d$  and  $C_k$  is reduced. The observed reduction in  $\sigma_{V_t}$  is because of both reduced uncertainty in the maximum  $V_t$  and in the reduced uncertainty of the RMW (Figs. 7a–e). In addition,  $\sigma_{V_t}$  is nearly identical with 1% systematic  $C_d$  and  $C_k$  uncertainty, stochastic  $C_d$  and  $C_k$  uncertainty, and Intrinsic uncertainty. Finally, before weakening/landfall,  $\sigma_{V_t}$  only becomes less than CV3 when the systematic uncertainty in  $C_d$  and  $C_k$  is reduced to 10%, consistent with previous results.

An additional metric often used to assess TC predictability is the dry total energy (DTE) (e.g., Zhang and Sippel 2009; Torn 2016). Azimuthally averaged DTE is calculated here as

$$\text{DTE}(r, z) = \frac{1}{N_{\text{ens}}} \sum_{n=1}^{N_{\text{ens}}} \left[ u(r, z)_n'^2 + v(r, z)_n'^2 + \frac{C_p}{T_r} T(r, z)_n'^2 \right], \quad (14)$$

where  $r$  is the radius,  $z$  is the height,  $N_{\text{ens}}$  is the number of ensemble members,  $u'$  is the perturbation radial wind ( $u' = u_n - \bar{u}$ , where  $\bar{u}$  is the ensemble mean radial wind and  $u_n$  is the ensemble member radial wind),  $v'$  is the perturbation tangential wind,  $T'$  is the perturbation temperature,  $C_p$  is the specific heat capacity of dry air, and  $T_r$  is the reference

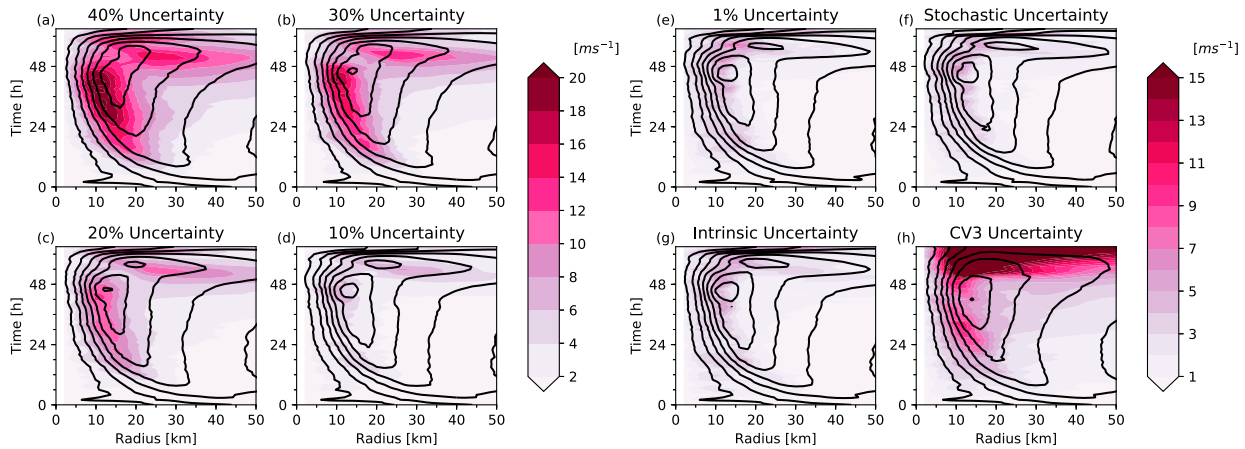


FIG. 7. Radius–time Hovmöller diagrams of azimuthally averaged tangential wind speed (shaded). The ensemble mean azimuthally averaged tangential wind speed is contoured every  $10 \text{ m s}^{-1}$ .

temperature ( $T_r = 300 \text{ K}$ ). For comparison, percentage difference DTE relative to CV3 is calculated at 36 h. Positive (negative) values denote greater (less) ensemble DTE variance relative to CV3. The change here to compare each ensemble directly with CV3 is chosen to emphasize the relative influence on inner-core error growth in comparison with that resulting from environmental IC uncertainty. The percent change in DTE variance can be interpreted as the difference in ensemble

variance relative to that caused by climatological environmental IC uncertainty.

The DTE with 40% systematic  $C_d$  and  $C_k$  uncertainty is over 200% greater than CV3 throughout the entire inner core (Fig. 8a). As the systematic  $C_d$  and  $C_k$  uncertainty is reduced to 30%, the percent difference in DTE relative to CV3 is still positive throughout nearly the entire inner core (Fig. 8b), indicating that ensemble DTE variance is much greater

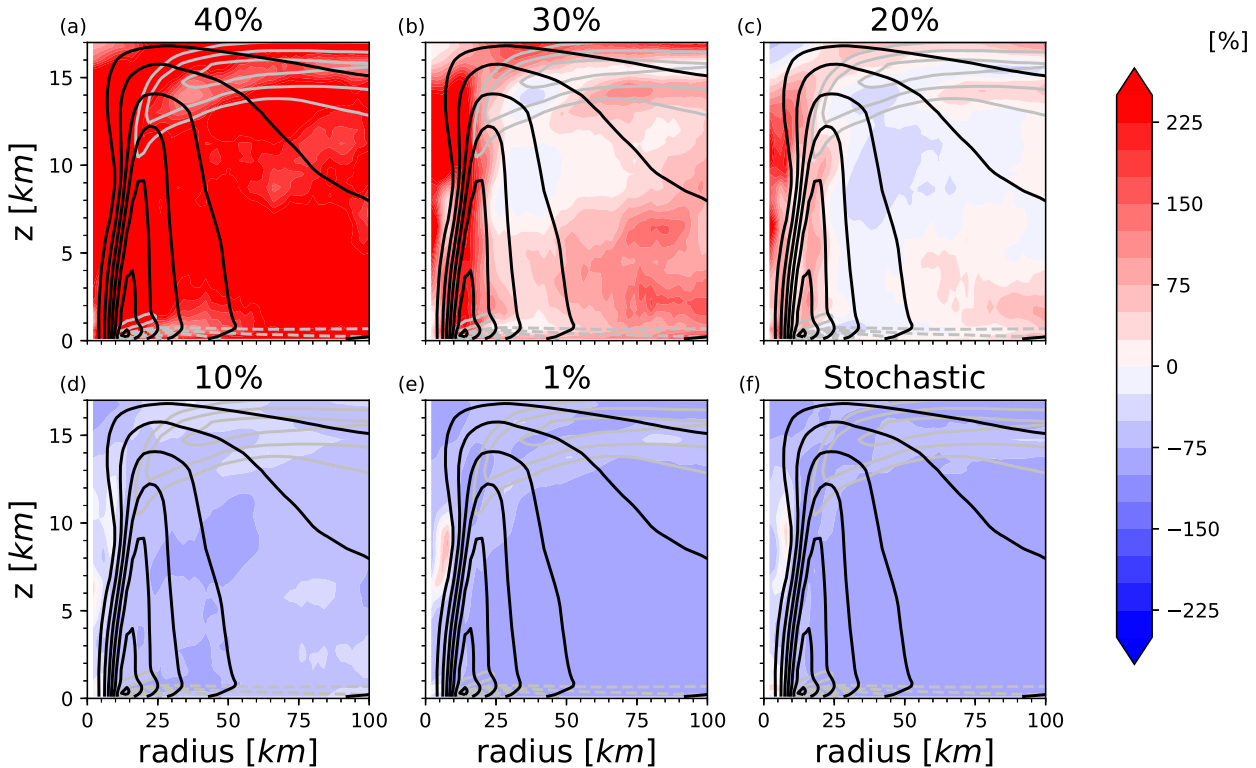


FIG. 8. Percentage change in DTE relative to CV3 uncertainty for (a) 40%, (b) 30%, (c) 20%, (d) 10%, and (e) 1% systematic and (f) stochastic uncertainties in  $C_d$  and  $C_k$  at 36 h. The black and gray contours highlight the ensemble mean tangential and radial winds every  $10$  and  $3 \text{ m s}^{-1}$ , respectively.

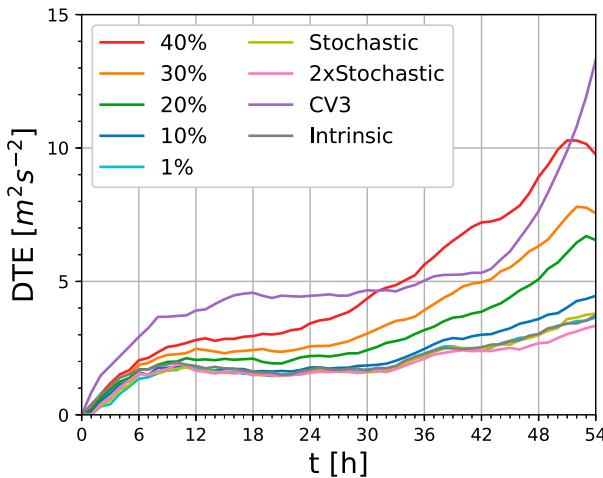


FIG. 9. Domain total DTE norm ( $10^7 \text{ m}^2 \text{ s}^{-2}$ ).

(>200%) with 30% systematic  $C_d$  and  $C_k$  uncertainty than CV3. One notable difference, in comparison with 40% systematic uncertainty, is that the greatest percent difference relative to CV3 is found primarily within the eyewall and beyond ~75 km with 30% systematic uncertainty. As the systematic  $C_d$  and  $C_k$  uncertainty is further reduced to 20%, the DTE variance is still 75% greater than CV3 within the eyewall and radially inward but is similar to CV3 radially outward of the eyewall (Fig. 8c). Once the systematic  $C_d$  and  $C_k$  uncertainty is reduced to 10%, the DTE percent difference becomes negative, indicating that ensemble DTE variance is now substantially (~50%–75%) less than CV3 (Fig. 8d). The negative percent change in TC inner-core DTE, relative to CV3, with 10% systematic  $C_d$  and  $C_k$  uncertainty further underlines the need to reduce current  $C_d$  and  $C_k$  uncertainty to reduce forecasting uncertainty for this case. Additional decrease in the systematic  $C_d$  and  $C_k$  uncertainty to 1% results in a further decrease in DTE variance relative to CV3 (>75%) throughout the entire inner core (Fig. 8e). Overall, continual reduction in systematic  $C_d$  and  $C_k$  uncertainty results in continuous DTE variance reduction throughout the TC inner core. Last, stochastically perturbing  $C_d$  and  $C_k$  results in substantially less DTE variance (>75%) throughout the entire inner core than CV3 (Fig. 8f). In other words, stochastically perturbing  $C_d$  and  $C_k$  again appears to have little influence on the simulated TC.

While systematic  $C_d$  and  $C_k$  perturbation cause the largest inner-core DTE, the domain total DTE (all model grid cells of the innermost domain, D04) is also calculated to highlight error growth associated with both the inner-core and the immediate near-storm environment. In addition, the domain total DTE—in combination with the inner-core DTE (Fig. 8)—also partially reveals the interactions between error growth in the near-storm environmental and TC inner-core region. The domain total DTE quickly increases for the first 6 h in all ensemble sets, with CV3 increasing the most rapidly (Fig. 9). CV3 has the largest domain total DTE through the first ~30 h, saturating at  $\sim 5 \times 10^7 \text{ m}^2 \text{ s}^{-2}$  before landfall uncertainty

increases DTE again. The large CV3 domain total DTE (Fig. 9) and the small inner-core DTE (Fig. 8) highlights that the error growth observed in CV3 is confined to the near-storm environment and does not strongly influence the inner core until near landfall. Beyond ~30 h, and before weakening/landfall, the largest domain total DTE is found with 40% systematic  $C_d$  and  $C_k$  uncertainty,  $\sim 7 \times 10^7 \text{ m}^2 \text{ s}^{-2}$  at 42 h (Fig. 9). The remainder of the ensemble sets always have smaller domain total DTE than CV3, likely because the TC is only a fraction of the total volume of D04, and CV3 directly perturbs the large-scale environment. Furthermore, the relatively small domain total DTE (Fig. 9) and the large inner-core DTE (Fig. 8) with systematic  $C_d$  and  $C_k$  perturbations highlight that  $C_d$  and  $C_k$  perturbations primarily influence the error growth within the TC inner core.

While the domain total DTE is less than CV3 when the systematic  $C_d$  and  $C_k$  uncertainty is 30% or less, the domain total DTE still decreases as the systematic uncertainty in  $C_d$  and  $C_k$  uncertainty is reduced (Fig. 9). In addition, the domain total DTE for all ensembles with systematic  $C_d$  and  $C_k$  uncertainty greater than 10% is noticeably greater than Intrinsic near the time of peak intensity (42 h), highlighting the substantial gap between the forecast uncertainty resulting from systematic  $C_d$  and  $C_k$  uncertainty and the intrinsic limit throughout the entirety of the innermost domain for this case. As the systematic  $C_d$  and  $C_k$  uncertainty is reduced from 10% to 1% the domain total DTE becomes nearly identical to Intrinsic, suggesting that one is approaching the intrinsic limit of predictability for this case. Finally, the domain total DTE in Stochastic and 2xStochastic is nearly identical to Intrinsic, regardless of the magnitude of stochastic  $C_d$  and  $C_k$  perturbations.

### c. Surface enthalpy and momentum flux uncertainty

TCS gain energy from the underlying warm ocean through latent and sensible heat transfer and lose momentum through surface friction. This balance between surface momentum and enthalpy fluxes largely explains TC intensification and the maximum intensity (e.g., Rotunno and Emanuel 1987; Emanuel 2012). From Eqs. (3) to (5) one can see that these surface fluxes are a function of the 10-m winds ( $V_{10}$  for sensible and latent heat and  $V_{10}^2$  for momentum), the respective disequilibrium with respect to the ocean surface, and the respective exchange coefficients. James de La Cruz et al. (2021) specifically demonstrated that increases in the thermodynamic disequilibrium or  $V_{10}$  could effectively increase the surface enthalpy fluxes and promote intensification. Ultimately, variability within each ensemble, except for CV3 and Intrinsic, is initially driven from systematic or stochastic  $C_d$  and  $C_k$  perturbations directly and subsequently from structural differences in the simulated TC (e.g.,  $V_{10}$ ,  $\Delta T$ , and  $\Delta q$ ), which in turn result from  $C_d$  and  $C_k$  differences. Therefore, variance in the model simulated surface enthalpy<sup>1</sup> and momentum fluxes should largely explain the simulated variance in TC intensity and structure. This should be especially true in this case as environmental

<sup>1</sup> The total surface enthalpy flux is calculated as the sum of the surface sensible and latent heat fluxes (KFLX = SH + LH).

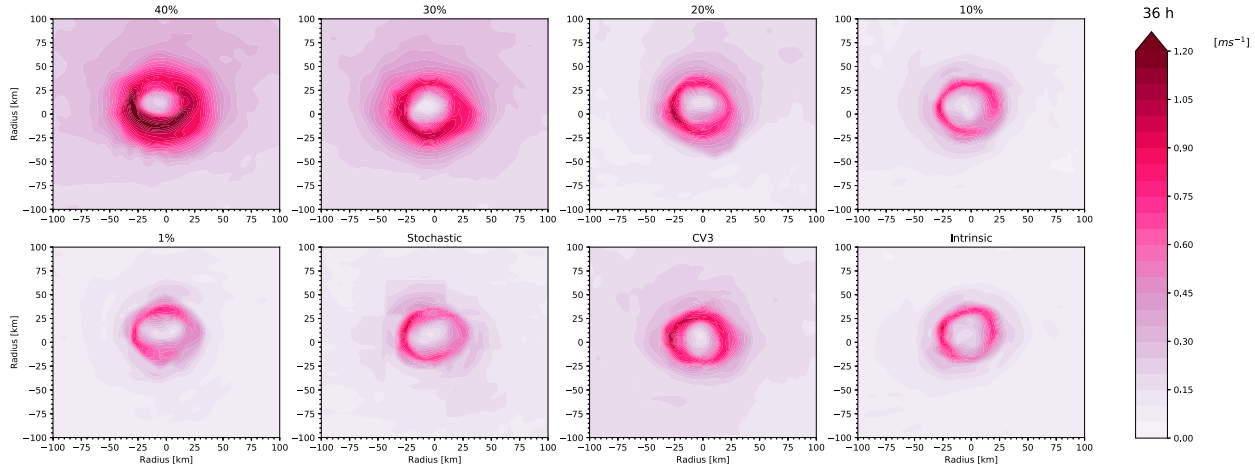


FIG. 10. Horizontal view of the ensemble standard deviation in friction velocity ( $u^*$ ) at 36 h.

conditions are very favorable (e.g., vertical wind shear is low and midlevel humidity is high).

To highlight the uncertainty within the surface fluxes in each ensemble, a 2D snapshot of the standard deviation of the friction velocity ( $u^*$ ) and surface enthalpy flux (KFLX) at 36 h is shown in Figs. 10 and 11, respectively. For all ensembles, the standard deviation of  $u^*$  and KFLX at 36 h is maximized within the eyewall where the wind speed is greatest. As expected, the standard deviation of  $u^*$  and KFLX decreases as the systematic uncertainty in  $C_d$  and  $C_k$  is reduced. This reduction in the standard deviation of  $u^*$  and KFLX is the result of both the direct reduction in  $C_d$  and  $C_k$  uncertainty and the reduction in wind speed uncertainty (intensity and structure), which is also related to the reduction in  $C_d$  and  $C_k$  uncertainty. In comparison to systematic  $C_d$  and  $C_k$  uncertainty, the stochastic standard deviation is between the ensembles with 20% and 10% systematic  $C_d$  and  $C_k$  uncertainty. In other words, there is still substantial uncertainty in  $u^*$  and KFLX at individual grid cells with stochastic  $C_d$  and  $C_k$  perturbations. However, this uncertainty is almost entirely the result of the

stochastic  $C_d$  and  $C_k$  perturbations, since the intensity and structure uncertainty is minimal (e.g., Figs. 4, 5, and 7). Furthermore, these stochastic perturbations to  $u^*$  and KFLX never appear to feedback to the storm scale and do not drive substantial differences in the overall TC intensity and structure, as will be further discussed next. Without prescribed  $C_d$  and  $C_k$  perturbations (CV3 and Intrinsic), uncertainty in  $u^*$  and KFLX still develops, because of uncertainty in simulated surface winds (Figs. 10 and 11). The  $u^*$  and KFLX standard deviations in CV3 are between 20% and 10% systematic  $C_d$  and  $C_k$  uncertainty, consistent with the uncertainty in TC intensity and structure becoming less than CV3 when systematic  $C_d$  and  $C_k$  uncertainty is reduced to 10% (e.g., Figs. 4, 5, and 7). Likewise, the  $u^*$  and KFLX standard deviations in Intrinsic appear comparable with 1% systematic  $C_d$  and  $C_k$  uncertainty.

More quantitatively, the average  $u^*$  and KFLX standard deviations within 50 km are calculated every hour for each ensemble ( $\overline{\sigma_{u^*}}$  and  $\overline{\sigma_{\text{KFLX}}}$ ). The standard deviations of  $u^*$  and KFLX are first calculated at every grid point from the innermost domain (D04) and then averaged within 50 km from the

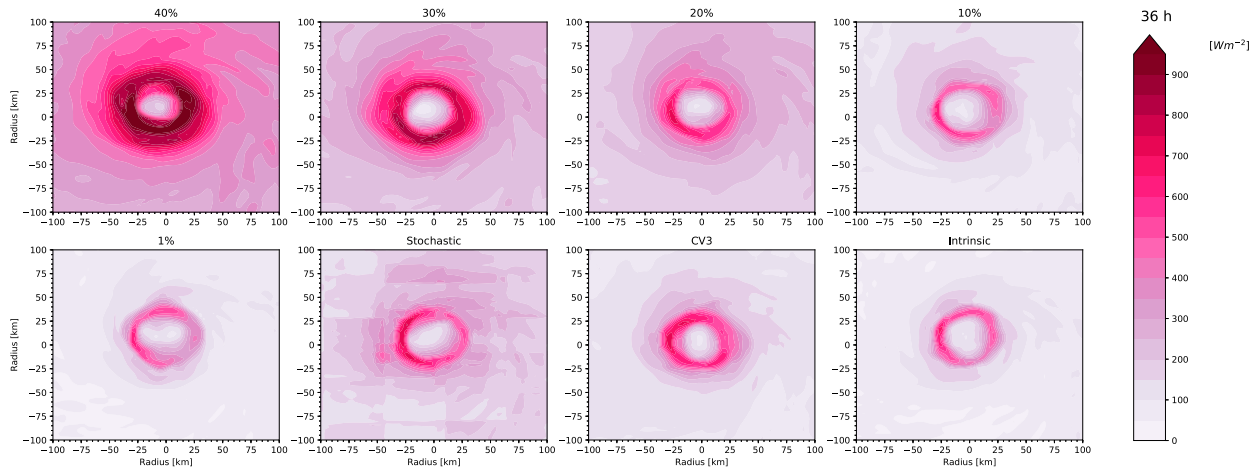


FIG. 11. Horizontal view of the ensemble standard deviation in enthalpy flux (KFLX) at 36 h.

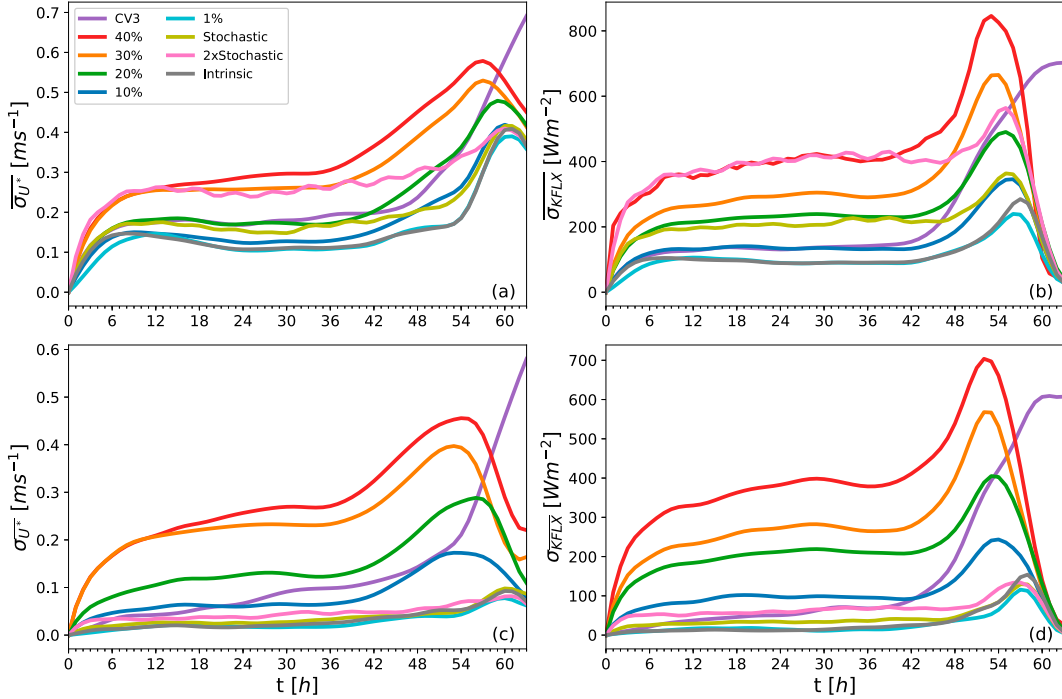


FIG. 12. (top) The average (left)  $u^*$  and (right) KFLX standard deviation within 50 km from TC center and (bottom) the standard deviation of the average (left)  $u^*$  and (right) KFLX within 50 km from TC center.

TC center, giving a quantitative measure of the average variability in  $u^*$  and KFLX within the inner core. In agreement with the 2-day snapshots of  $u^*$  and KFLX standard deviation at 36 h in Figs. 10 and 11, the average inner-core variability in  $u^*$  and KFLX decreases as the systematic uncertainty in  $C_d$  and  $C_k$  is reduced from 40% to 1% (Figs. 12a,b). Additionally,  $\bar{\sigma}_{u^*}$  and  $\bar{\sigma}_{KFLX}$  with 1% systematic  $C_d$  and  $C_k$  uncertainty is nearly identical to Intrinsic at all forecast times and  $\bar{\sigma}_{u^*}$  and  $\bar{\sigma}_{KFLX}$  become less than CV3 once the systematic uncertainty in  $C_d$  and  $C_k$  is reduced to 10%. Last,  $\bar{\sigma}_{u^*}$  and  $\bar{\sigma}_{KFLX}$  increase as the magnitude of the stochastic perturbations is increased. More specifically, the magnitude of  $\bar{\sigma}_{u^*}$  is similar to 20% (30%) systematic  $C_d$  and  $C_k$  uncertainty in Stochastic (2xStochastic) and the magnitude of  $\bar{\sigma}_{KFLX}$  is similar to 20% (40%) systematic  $C_d$  and  $C_k$  uncertainty in Stochastic (2xStochastic).

To better quantify variability in the axisymmetric fluxes, the standard deviation of the average  $u^*$  and KFLX within 50 km is calculated at all forecast times ( $\sigma_{\bar{u}^*}$  and  $\sigma_{\bar{KFLX}}$ ). The quantities  $u^*$  and KFLX are first averaged within 50 km from the TC center for each ensemble member and then the standard deviation is calculated for each ensemble set. While both systematically and stochastically perturbing  $C_d$  and  $C_k$  resulted in substantial inner-core variability in  $u^*$  and KFLX (Figs. 12a,b), our theoretical understanding of TC intensification depends on the axisymmetric surface fluxes beneath the eyewall, which dominate owing to the large wind speeds found in this region (e.g., Emanuel 1988). In addition, some energy exchange beyond the eyewall, as the air spirals radially inward at the surface, may also be important (e.g., Wang and Xu 2010; Kowaleski and Evans 2016). By first averaging  $u^*$  and KFLX within 50 km of the

TC center for each ensemble member and then taking the standard deviation we hope to better highlight the role of the cumulative inner-core surface fluxes in driving the simulated variability in TC intensity and structure.

Consistent with the average  $u^*$  and KFLX variability within the inner core (Figs. 12a,b),  $\sigma_{\bar{u}^*}$  and  $\sigma_{\bar{KFLX}}$  decrease as the systematic uncertainty in  $C_d$  and  $C_k$  is reduced from 40% to 1% (Figs. 12c,d). This suggests that as the systematic uncertainty in  $C_d$  and  $C_k$  is reduced, the reduction in average inner-core  $u^*$  and KFLX variability ( $\bar{\sigma}_{u^*}$  and  $\bar{\sigma}_{KFLX}$ ) projects onto the variability of the average inner-core  $u^*$  and KFLX ( $\sigma_{\bar{u}^*}$  and  $\sigma_{\bar{KFLX}}$ ). The same behavior is not found in Stochastic and 2xStochastic, which has  $\sigma_{\bar{u}^*}$  and  $\sigma_{\bar{KFLX}}$  nearly equivalent to Intrinsic in both cases. This strongly suggests that the variability of the average inner-core  $u^*$  and KFLX, which is only substantially perturbed with systematic  $C_d$  and  $C_k$  perturbations, better explains the observed forecasted intensity and structure uncertainty. In other words, unless the  $u^*$  and KFLX uncertainty alters the cumulative inner-core surface fluxes, the perturbations have minimal influence on the simulated TC intensity or structure.

#### d. Scale-dependent predictability analysis

TCs comprise a range of scales, extending from small-scale turbulence  $O(<1)$  m to the eyewall  $O(10)$  km and storm scale  $O(1000)$  km. To understand how errors grow in our various ensembles across scales, the surface (10-m) wind speed is decomposed into azimuthal wavenumbers and the mean KE error spectra [ $E(k)$ ] averaged throughout the TC is compared to the mean KE [KE( $k$ )], as in Judt et al. (2015). The process

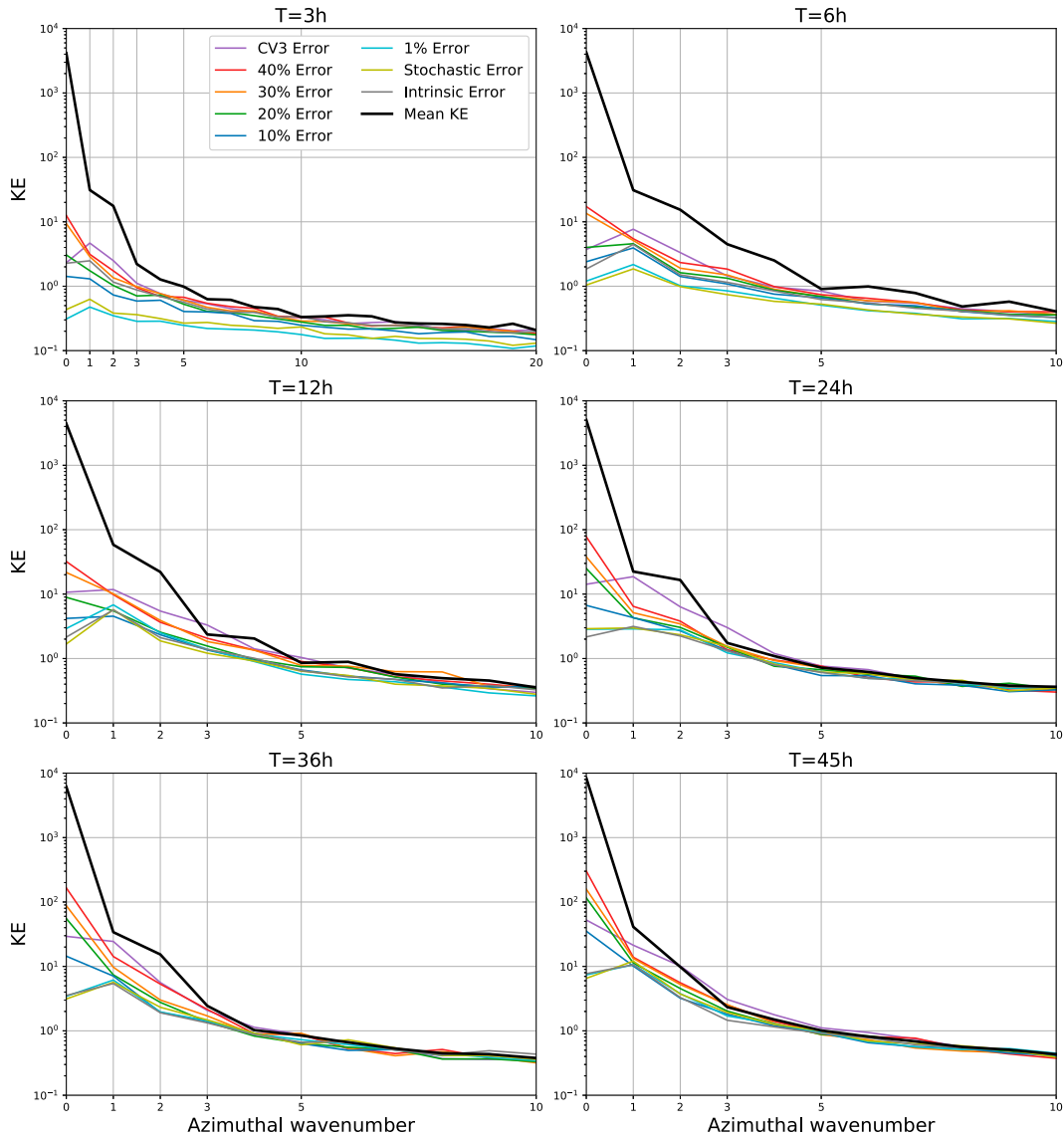


FIG. 13. Storm-scale-averaged KE power spectrum for each ensemble at 3, 6, 12, 24, 36, and 45 h.

of averaging the Fourier-decomposed azimuthal KE error and mean KE throughout the TC [within 150 km from the TC center; Eqs. (9) and (10)] will be referred to hereafter as the storm-scale predictability. Recall that, according to our theoretical understanding, a given wavenumber ( $k$ ) loses predictability when  $\bar{E}(k) = 2\text{KE}(k)$  (Lorenz 1969). This process is also referred to as error saturation and is visible in the subsequent figures approximately when the  $\bar{E}(k)$  curve lies roughly on-top-of the  $\text{KE}(k)$  curve. Last, while our simulated TC is never in statistical equilibrium and the KE is increasing as the storm intensifies, errors still appear to saturate at some wavenumbers and  $\bar{E}(k)$  subsequently grows in magnitude with  $\text{KE}(k)$  thereafter.

In all ensembles, storm-scale errors in KE quickly develop and amplify at all wavenumbers beginning at the first-time step. Even after only a few hours, wavenumbers higher than

$\sim 10$  have already lost predictability (error is saturated; Fig. 13), consistent with Judt et al. (2015). Focusing on wavenumbers 0–10, the storm-scale predictability is lost for wavenumbers 5–10 by 12 h and wavenumbers 3–10 by 24 h. This suggests that storm-scale predictability of the KE associated with wavenumbers 3 and higher is intrinsically limited to  $\sim 1$  day for this case, regardless of the ensemble design.

While predictability is lost for wavenumbers 3 and higher by 24 h in all ensembles, there are visible differences in the error growth of wavenumbers 0–2 between the ensembles at 24 h (Fig. 13). Starting with wavenumber 0,  $\bar{E}(0)$  is the greatest with 40% systematic  $C_d$  and  $C_k$  uncertainty. Additionally, as the systematic  $C_d$  and  $C_k$  uncertainty is reduced from 40% to 1%,  $\bar{E}(0)$  is also reduced. Furthermore, at 24 h, the storm-scale  $\bar{E}(0)$  is greater than CV3 with 40%, 30%, and 20% systematic  $C_d$  and  $C_k$  uncertainty, consistent with the uncertainty

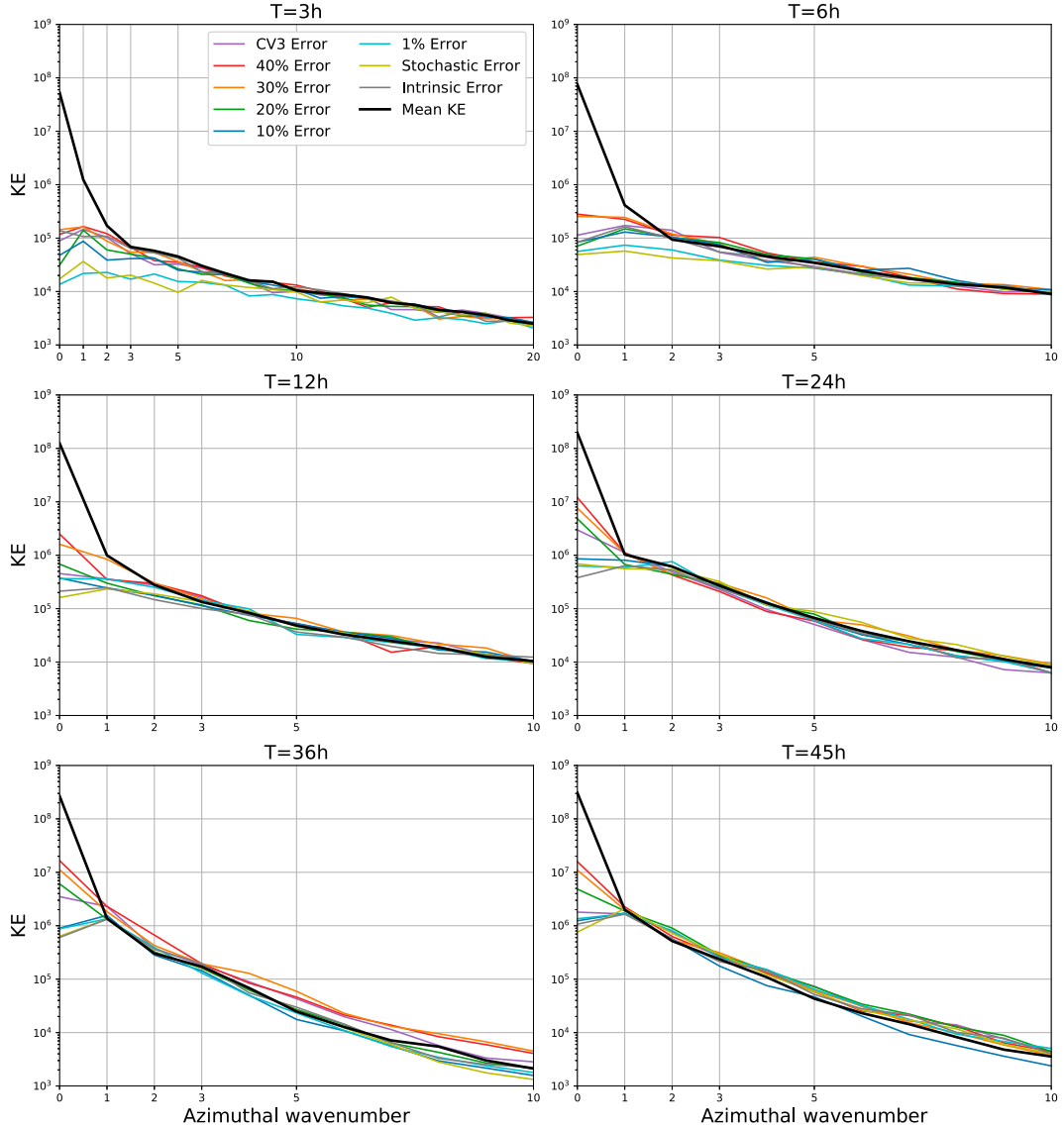


FIG. 14. Eyewall-averaged (RMW  $\pm$  4 km) KE power spectrum for each ensemble at 3, 6, 12, 24, 36, and 45 h.

in pointwise intensity metrics (Fig. 4). When the systematic  $C_d$  and  $C_k$  uncertainty is reduced to 10%, the storm-scale  $\bar{E}(0)$  becomes less than CV3 (Fig. 13). Further reducing the systematic  $C_d$  and  $C_k$  uncertainty to 1% results in  $\bar{E}(0)$  comparable with Stochastic and Intrinsic. For wavenumbers 1 and 2,  $\bar{E}(1-2)$  has not yet saturated by 24 h for any of the ensembles, but the greatest storm-scale  $\bar{E}(1-2)$  is found with CV3 (Fig. 13). CV3 likely has the largest  $\bar{E}(1-2)$  because uncertainty in environmental conditions cause the most rapid error growth in TC rainband activity, which project strongly onto wavenumbers 1 and 2. Last, while the greatest storm-scale  $\bar{E}(1-2)$  is found in CV3, a reduction in  $\bar{E}(1-2)$  with reduced  $C_d$  and  $C_k$  uncertainty is still evident and  $\bar{E}(1-2)$  from Stochastic is comparable to Intrinsic.

As the simulated TC further intensifies and approaches the time of maximum intensity ( $\sim$ 45 h), the storm-scale

$\bar{E}(1-2)$  continues to increase in all ensembles, but never becomes saturated for wavenumbers 0 and 1 for any of the ensembles and only saturates with CV3 for wavenumber 2 at  $\sim$ 45 h (Fig. 13). The fact that  $\bar{E}(0-1)$  never saturates by 45 h is consistent with Judt et al. (2015) and suggests that these scales remain predictable throughout Patricia's life cycle. One additional unexpected result is that the greatest  $\bar{E}(0)$  is found with 40% systematic  $C_d$  and  $C_k$  uncertainty but the greatest  $\bar{E}(1-2)$  is found in CV3. This relative difference in  $\bar{E}(0)$  and  $\bar{E}(1-2)$  suggests that systematic  $C_d$  and  $C_k$  uncertainty projects strongly onto wavenumber 0 and the overall intensity of the storm, but projects less strongly onto wavenumbers 1 and 2 in comparison with environmental condition uncertainty in this case. Furthermore, it also suggests that the greater  $\bar{E}(1-2)$  in CV3 does not grow upscale to strongly influence  $\bar{E}(0)$ .

Comparing with CV3, the storm-scale  $\overline{E(0)}$ , for the period through maximum intensity, only becomes less than CV3 once systematic  $C_d$  and  $C_k$  uncertainty is reduced to 10%. This further suggests that reducing the systematic  $C_d$  and  $C_k$  uncertainty to 10% is necessary to reduce  $\overline{E(0)}$  to less than that generated from CV3 uncertainty (Fig. 13). Finally, Stochastic continues to result in similar  $\overline{E(k)}$  growth as Intrinsic at all scales and times. The similar  $\overline{E(k)}$  growth from Stochastic and Intrinsic further highlights that stochastically perturbing  $C_d$  and  $C_k$  only has the same influence on simulated TC structure uncertainty as random boundary layer moisture perturbations (Intrinsic). Stochastically perturbing  $C_d$  and  $C_k$  is therefore not an adequate approach to account for the influences of  $C_d$  and  $C_k$  uncertainty on TC prediction in numerical models.

In many ways, averaging the KE spectrum over the entire TC (within 150 km from the center) is not the most representative of TC intensity predictability. A potentially more representative way to link the classical turbulence prospective on predictability to TC intensity is to analyze the KE spectrum within the eyewall only, in the immediate vicinity of the RMW [ $\pm 4$  km; Eqs. (12) and (13)].

When averaged within the eyewall, instead of over the entire TC, errors are saturated for wavenumbers greater than 3 in all ensembles by 6–12 h (Fig. 14). By 24 h errors are saturated at all wavenumbers except wavenumber 0. This suggests that the eyewall KE, except for the azimuthal mean ( $k = 0$ ), is unpredictable beyond 24 h in all ensembles. Only the azimuthal mean eyewall KE remains predictable in all ensembles. Despite the eyewall azimuthal mean KE always remaining predictable,  $\overline{E_m(0)}$  still increases as the systematic uncertainty in  $C_d$  and  $C_k$  increases. In addition,  $\overline{E_m(0)}$  again becomes less than CV3 only once the systematic  $C_d$  and  $C_k$  uncertainty is reduced from 20% to 10%. Some of the largest relative reduction in  $\overline{E_m(0)}$  is found when the systematic  $C_d$  and  $C_k$  uncertainty is reduced from 20% to 10%, consistent with pointwise intensity metrics (Figs. 3 and 4). Finally, stochastically perturbing  $C_d$  and  $C_k$  results in similar  $\overline{E_m(0)}$  as Intrinsic. Overall, the error growth of eyewall KE is similar to the storm-scale error growth for  $k = 0$  and more rapid for  $k \geq 0$ .

#### 4. Summary and conclusions

The surface-exchange coefficients are highly uncertain at high wind speeds and are well-known to influence TC intensity and structure. In this study we quantify the influences of surface-exchange coefficient uncertainty on the predictability of Hurricane Patricia (2015), an extremely intense TC but also a TC with high intrinsic predictability given the favorable environmental conditions. We conducted nine 20-member ensembles with either systematic  $C_d$  and  $C_k$  uncertainty (40%, 30%, 20%, 10%, or 1%), stochastic  $C_d$  and  $C_k$  perturbations, CV3 climatological environmental IC uncertainty, or small boundary layer water vapor mixing ratio perturbations. This approach allows for a systematic comparison of the error growth resulting from (i) different magnitudes of systematic  $C_d$  and  $C_k$  perturbations, (ii) differences between systematically and stochastically perturbing  $C_d$  and  $C_k$ , (iii) environmental IC uncertainty, and

(iv) the intrinsic limit for this case. While only a single case, the results of this study are likely applicable to other strong TCs which rapidly intensify under favorable environmental conditions. The primary conclusions are as follows:

- 1) As the systematic uncertainty in  $C_d$  and  $C_k$  is reduced from 40% to 1% the simulated intensity and structure uncertainty are substantially reduced.
- 2) The forecasted intensity and structure uncertainty are larger than that caused by environmental IC uncertainty until the systematic uncertainty in  $C_d$  and  $C_k$  is reduced to 10%.
- 3) Perturbing  $C_d$  and  $C_k$  stochastically, instead of systematically, results in minimal intensity and structure uncertainty, which is similar to the intrinsic limit for this case regardless of the magnitude of the stochastic perturbations.
- 4) The lack of uncertainty in the area-averaged surface momentum and enthalpy fluxes when  $C_d$  and  $C_k$  are perturbed stochastically limits simulated intensity and structure uncertainty.
- 5) While errors rapidly grow and saturate on small scales in all ensembles, azimuthal wavenumber 0 KE errors never saturate on either the storm-scale or within the eyewall in any ensembles, suggesting the azimuthal mean KE error is resilient to upscale energy growth. Wavenumber 0 KE errors are, however, still maximized when  $C_d$  and  $C_k$  are perturbed systematically.

The substantial reduction in intensity uncertainty as the uncertainty in  $C_d$  and  $C_k$  is reduced highlights the gains in predictability possible by reducing current surface-exchange coefficient uncertainties. As the systematic uncertainty in  $C_d$  and  $C_k$  is reduced from 40% to 1% the simulated standard deviation in  $V_{\max}$  ( $P_{\min}$ ) near peak intensity is substantially reduced from  $15 \text{ m s}^{-1}$  (35 hPa) to  $2 \text{ m s}^{-1}$  (3 hPa). Additionally, the fact that uncertainty in  $V_{\max}$  and  $P_{\min}$  caused by environmental IC uncertainty is smaller than that caused by systematic  $C_d$  and  $C_k$  uncertainty, until reduced to 10%, suggests the practical predictability of other strong TCs can likely also be improved by reducing  $C_d$  and  $C_k$  uncertainty. Furthermore, because perturbing  $C_d$  and  $C_k$  stochastically at every model grid point and time step has minimal influence on simulated intensity (the intensity uncertainty is similar to the intrinsic limit for this case), stochastic perturbations on small spatial and temporal scales do not appear to be an appropriate approach to account for the influences of this uncertain physical process on TC prediction. Like intensity, simulated TC structure uncertainty is similarly influenced by  $C_d$  and  $C_k$  uncertainty and is not strongly influenced when  $C_d$  and  $C_k$  are perturbed stochastically.

The strong influence of systematic  $C_d$  and  $C_k$  perturbations and the minimal influence of stochastic  $C_d$  and  $C_k$  perturbations on simulated TC intensity are consistent with the results of Torn (2016) which analyzed the average influence on 20 Atlantic TCs over a 4-yr period. In contrast with Torn (2016), however, our results highlight the dominant influence systematic  $C_d$  and  $C_k$  perturbations can have in limiting the practical predictability of a TC under favorable environmental conditions. In addition, the apparent insensitivity to stochastic  $C_d$  and  $C_k$

perturbations raises additional questions on the potential importance of ocean waves in modulating TC intensity, through larger temporal- and spatial-scale perturbations on  $C_d$  and  $C_k$  (e.g., Moon et al. 2004a,b; Chen et al. 2020).

Consistent with hurricane Earl (2010; Judt et al. 2015), the KE error growth is generally described by simultaneous error growth at all scales. Furthermore, errors quickly saturate for small scales but azimuthal wavenumbers 0 and 1 remain predictable for the storm-scale throughout Patricia's intensification. In addition to the storm-scale KE error growth, it is also shown that only the azimuthal wavenumber 0 remains predictable for the eyewall region beyond  $\sim 24$  h. This apparent predictability of the azimuthal mean maximum wind speed throughout Patricia's intensification appears to differ with the loss of predictability by  $\sim 48$  h found in the idealized simulations of Brown and Hakim (2013). This difference in predictability may result from either environmental conditions, which provide predictability for the azimuthal mean, and/or differences in the predictability between the intensification phase and the steady-state period. We leave such an explanation to future work.

While this study highlights the relatively strong influence that  $C_d$  and  $C_k$  uncertainty can have on TC predictability, it is important to acknowledge that only one TC and a single initialization time are presented here. It is possible that different initialization times may reveal stronger or weaker sensitivities to  $C_d$  and  $C_k$  perturbations. In addition, other TCs—and specifically those with less favorable environmental conditions—may have differing relative sensitivities to  $C_d$  and  $C_k$ . Nevertheless, this study reinforces the importance of ongoing efforts to reduce current surface-exchange coefficient uncertainties and highlights the positive influence those efforts could have in improving TC intensity predictions.

**Acknowledgments.** This material is based upon work supported by the National Center for Atmospheric Research (NCAR), which is a major facility sponsored by the National Science Foundation under Cooperative Agreement 1852977. Computing Resources were provided by NCAR's Computational and Information Systems Laboratory (CISL) and the Texas Advanced Computing Center (TACC). We are also grateful to Richard R. Rotunno and George H. Bryan for an initial review of an earlier draft of this manuscript. Finally, we thank two anonymous reviewers that helped to improve the quality of this manuscript.

**Data availability statement.** We provide all the information needed to replicate the numerical model simulations upon which this study is based. We used WRF Model version 3.9.1. Furthermore, the model code, initial, and boundary conditions and the namelist settings are available at DOI (<https://doi.org/10.5065/aynt-tn92>).

## REFERENCES

- Bell, M. M., M. T. Montgomery, and K. A. Emanuel, 2012: Air-sea enthalpy and momentum exchange at major hurricane wind speeds observed during CBLAST. *J. Atmos. Sci.*, **69**, 3197–3222, <https://doi.org/10.1175/JAS-D-11-0276.1>.
- Bender, M. A., I. Ginis, and Y. Kurihara, 1993: Numerical simulations of tropical cyclone–ocean interaction with a high-resolution coupled model. *J. Geophys. Res.*, **98**, 23 245–23 263, <https://doi.org/10.1029/93JD02370>.
- Brown, B. R., and G. J. Hakim, 2013: Variability and predictability of a three-dimensional hurricane in statistical equilibrium. *J. Atmos. Sci.*, **70**, 1806–1820, <https://doi.org/10.1175/JAS-D-12-0112.1>.
- Chen, X., T. Hara, and I. Ginis, 2020: Impact of shoaling ocean surface waves on wind stress and drag coefficient in coastal waters: 1. Uniform wind. *J. Geophys. Res. Oceans*, **125**, e2020JC016222, <https://doi.org/10.1029/2020JC016222>.
- Curcic, M., and B. K. Haus, 2020: Revised estimates of ocean surface drag in strong winds. *Geophys. Res. Lett.*, **47**, e2020GL087647, <https://doi.org/10.1029/2020GL087647>.
- Davis, C., and Coauthors, 2008: Prediction of landfalling hurricanes with the Advanced Hurricane WRF Model. *Mon. Wea. Rev.*, **136**, 1990–2005, <https://doi.org/10.1175/2007MWR2085.1>.
- Emanuel, K. A., 1988: The maximum intensity of hurricanes. *J. Atmos. Sci.*, **45**, 1143–1155, [https://doi.org/10.1175/1520-0469\(1988\)045<1143:TMIOH>2.0.CO;2](https://doi.org/10.1175/1520-0469(1988)045<1143:TMIOH>2.0.CO;2).
- , 1997: Some aspects of hurricane inner-core dynamics and energetics. *J. Atmos. Sci.*, **54**, 1014–1026, [https://doi.org/10.1175/1520-0469\(1997\)054<1014:SAOHC>2.0.CO;2](https://doi.org/10.1175/1520-0469(1997)054<1014:SAOHC>2.0.CO;2).
- , 2012: Self-stratification of tropical cyclone outflow. Part II: Implications for storm intensification. *J. Atmos. Sci.*, **69**, 988–996, <https://doi.org/10.1175/JAS-D-11-0177.1>.
- , and F. Zhang, 2016: On the predictability and error sources of tropical cyclone intensity forecasts. *J. Atmos. Sci.*, **73**, 3739–3747, <https://doi.org/10.1175/JAS-D-16-0100.1>.
- , and —, 2017: The role of inner core moisture in tropical cyclone predictability and practical forecast skill. *J. Atmos. Sci.*, **74**, 2315–2324, <https://doi.org/10.1175/JAS-D-17-0008.1>.
- Fox, R. K., and F. Judt, 2018: A numerical study on the extreme intensification of Hurricane Patricia (2015). *Wea. Forecasting*, **33**, 989–999, <https://doi.org/10.1175/WAF-D-17-0101.1>.
- Green, B. W., and F. Zhang, 2013: Impacts of air-sea flux parameterizations on the intensity and structure of tropical cyclones. *Mon. Wea. Rev.*, **141**, 2308–2324, <https://doi.org/10.1175/MWR-D-12-00274.1>.
- Hsu, J. Y., R. C. Lien, E. A. D'Asaro, and T. B. Sanford, 2019: Scaling of drag coefficients under five tropical cyclones. *Geophys. Res. Lett.*, **46**, 3349–3358, <https://doi.org/10.1029/2018GL081574>.
- James de La Cruz, B. J., L. K. Shay, J. B. Wadler, and J. E. Rudzin, 2021: On the hyperbolicity of the bulk air-sea heat flux functions: Insights into the efficiency of air-sea moisture disequilibrium for tropical cyclone intensification. *Mon. Wea. Rev.*, **149**, 1517–1534, <https://doi.org/10.1175/MWR-D-20-0324.1>.
- Jarosz, E., D. A. Mitchell, D. W. Wang, and W. J. Teague, 2007: Bottom-up determination of air-sea momentum exchange under a major tropical cyclone. *Science*, **315**, 1707–1709, <https://doi.org/10.1126/science.1136466>.
- Judt, F., S. S. Chen, and J. Berner, 2015: Predictability of tropical cyclone intensity: Scale-dependent forecast error growth in high-resolution stochastic kinetic-energy backscatter ensembles. *Quart. J. Roy. Meteor. Soc.*, **142**, 43–57, <https://doi.org/10.1002/qj.2626>.

- Kieu, C. Q., and Z. Moon, 2016: Hurricane intensity predictability. *Bull. Amer. Meteor. Soc.*, **97**, 1847–1857, <https://doi.org/10.1175/BAMS-D-15-00168.1>.
- Kimberlain, T. B., E. S. Blake, and J. P. Cangialosi, 2016: National Hurricane Center tropical cyclone report: Hurricane Patricia (20–24 October 2015). National Hurricane Center Tropical Cyclone Rep. EP202015, 32 pp., [https://www.nhc.noaa.gov/data/tcr/EP202015\\_Patricia.pdf](https://www.nhc.noaa.gov/data/tcr/EP202015_Patricia.pdf).
- Komori, S., K. Iwano, N. Takagaki, R. Onishi, R. Kurose, K. Takahashi, and N. Suzuki, 2018: Laboratory measurements of heat transfer and drag coefficients at extremely high wind speeds. *J. Phys. Oceanogr.*, **48**, 959–974, <https://doi.org/10.1175/JPO-D-17-0243.1>.
- Kowaleski, A. M., and J. L. Evans, 2016: A reformulation of tropical cyclone potential intensity theory incorporating energy production along a radial trajectory. *Mon. Wea. Rev.*, **144**, 3569–3578, <https://doi.org/10.1175/MWR-D-15-0383.1>.
- Lorenz, E. N., 1969: The predictability of a flow which possesses many scales of motion. *Tellus*, **21**, 289–307, <https://doi.org/10.3402/tellusa.v21i3.10086>.
- Moon, I.-J., I. Ginis, and T. Hara, 2004a: Effect of surface waves on air-sea momentum exchange. Part II: Behavior of drag coefficient under tropical cyclones. *J. Atmos. Sci.*, **61**, 2334–2348, [https://doi.org/10.1175/1520-0469\(2004\)061<2334:EOSWOA>2.0.CO;2](https://doi.org/10.1175/1520-0469(2004)061<2334:EOSWOA>2.0.CO;2).
- , —, and —, 2004b: Effect of surface waves on Charnock coefficient under tropical cyclones. *Geophys. Res. Lett.*, **31**, L20302, <https://doi.org/10.1029/2004GL020988>.
- Nystrom, R. G., and F. Zhang, 2019: Practical uncertainties in the limited predictability of the record-breaking intensification of Hurricane Patricia (2015). *Mon. Wea. Rev.*, **147**, 3535–3556, <https://doi.org/10.1175/MWR-D-18-0450.1>.
- , —, E. B. Munsell, S. A. Braun, J. A. Sippel, Y. Weng, and K. Emanuel, 2018: Predictability and dynamics of Hurricane Joaquin (2015) explored through convection-permitting ensemble sensitivity experiments. *J. Atmos. Sci.*, **75**, 401–424, <https://doi.org/10.1175/JAS-D-17-0137.1>.
- , X. Chen, F. Zhang, and C. A. Davis, 2020a: Nonlinear impacts of surface exchange coefficient uncertainty on tropical cyclone intensity and air-sea interactions. *Geophys. Res. Lett.*, **47**, e2019GL085783, <https://doi.org/10.1029/2019GL085783>.
- , R. Rotunno, C. A. Davis, and F. Zhang, 2020b: Consistent impacts of surface enthalpy and drag coefficient uncertainty between an analytical model and simulated tropical cyclone maximum intensity and storm structure. *J. Atmos. Sci.*, **77**, 3059–3080, <https://doi.org/10.1175/JAS-D-19-0357.1>.
- , S. J. Greybush, X. Chen, and F. Zhang, 2021: Potential for new constraints on tropical cyclone surface-exchange coefficients through simultaneous ensemble-based state and parameter estimation. *Mon. Wea. Rev.*, **149**, 2213–2230, <https://doi.org/10.1175/MWR-D-20-0259.1>.
- Ooyama, K. V., 1969: Numerical simulation of the life cycle of tropical cyclones. *J. Atmos. Sci.*, **26**, 3–40, [https://doi.org/10.1175/1520-0469\(1969\)026<0003:NSOTLC>2.0.CO;2](https://doi.org/10.1175/1520-0469(1969)026<0003:NSOTLC>2.0.CO;2).
- Powell, M. D., and T. A. Reinhold, 2007: Tropical cyclone destructive potential by integrated kinetic energy. *Bull. Amer. Meteor. Soc.*, **88**, 513–526, <https://doi.org/10.1175/BAMS-88-4-513>.
- Qin, N., and D.-L. Zhang, 2018: On the extraordinary intensification of Hurricane Patricia (2015). Part I: Numerical experiments. *Wea. Forecasting*, **33**, 1205–1224, <https://doi.org/10.1175/WAF-D-18-0045.1>.
- Richter, D. H., R. Bohac, and D. P. Stern, 2016: An assessment of the flux profile method for determining air-sea momentum and enthalpy fluxes from dropsonde data in tropical cyclones. *J. Atmos. Sci.*, **73**, 2665–2682, <https://doi.org/10.1175/JAS-D-15-0331.1>.
- , C. Wainwright, D. P. Stern, G. H. Bryan, and D. Chavas, 2021: Potential low bias in high-wind drag coefficient inferred from dropsonde data in hurricanes. *J. Atmos. Sci.*, **78**, 2339–2352, <https://doi.org/10.1175/JAS-D-20-0390.1>.
- Rogers, R. F., and Coauthors, 2017: Rewriting the tropical record books: The extraordinary intensification of Hurricane Patricia (2015). *Bull. Amer. Meteor. Soc.*, **98**, 2091–2112, <https://doi.org/10.1175/BAMS-D-16-0039.1>.
- Rotunno, R., and K. A. Emanuel, 1987: An air-sea interaction theory for tropical cyclones. Part II: Evolutionary study using a nonhydrostatic axisymmetric numerical model. *J. Atmos. Sci.*, **44**, 542–561, [https://doi.org/10.1175/1520-0469\(1987\)044<0542:AAITFT>2.0.CO;2](https://doi.org/10.1175/1520-0469(1987)044<0542:AAITFT>2.0.CO;2).
- , and C. Snyder, 2008: A generalization of Lorenz's model for the predictability of flows with many scales of motion. *J. Atmos. Sci.*, **65**, 1063–1076, <https://doi.org/10.1175/2007JAS2449.1>.
- Sanford, T. B., P. G. Black, J. R. Haustein, J. W. Feeney, G. Z. Forristall, and J. F. Price, 1987: Ocean response to a hurricane. Part I: Observations. *J. Phys. Oceanogr.*, **17**, 2065–2083, [https://doi.org/10.1175/1520-0485\(1987\)017<2065:ORTAHP>2.0.CO;2](https://doi.org/10.1175/1520-0485(1987)017<2065:ORTAHP>2.0.CO;2).
- Skamarock, W. C., and Coauthors, 2008: A description of the Advanced Research WRF version 3. NCAR Tech. Note NCAR/TN-475+STR, 113 pp., <https://doi.org/10.5065/D68S4MVH>.
- Sroka, S., and K. Emanuel, 2021: A review of parameterizations for enthalpy and momentum fluxes from sea spray in tropical cyclones. *J. Phys. Oceanogr.*, **51**, 3053–3069, <https://doi.org/10.1175/JPO-D-21-0023.1>.
- Tao, D., and F. Zhang, 2015: Effects of vertical wind shear on the predictability of tropical cyclones: Practical versus intrinsic limit. *J. Adv. Model. Earth Syst.*, **7**, 1534–1553, <https://doi.org/10.1002/2015MS000474>.
- Torn, R. D., 2016: Evaluation of atmosphere and ocean initial condition uncertainty and stochastic exchange coefficients on ensemble tropical cyclone intensity forecasts. *Mon. Wea. Rev.*, **144**, 3487–3506, <https://doi.org/10.1175/MWR-D-16-0108.1>.
- , and D. Cook, 2013: The role of vortex and environment errors in genesis forecasts of Hurricanes Danielle and Karl (2010). *Mon. Wea. Rev.*, **141**, 232–251, <https://doi.org/10.1175/MWR-D-12-00086.1>.
- Troitskaya, Y., D. Sergeev, M. Vdovin, A. Kandaurov, O. Ermakova, and N. Takagaki, 2020: A laboratory study of the effect of surface waves on heat and momentum transfer at high wind speeds. *J. Geophys. Res. Oceans*, **125**, e2020JC016276, <https://doi.org/10.1029/2020JC016276>.
- Van Sang, N., R. K. Smith, and M. T. Montgomery, 2008: Tropical-cyclone intensification and predictability in three dimensions. *Quart. J. Roy. Meteor. Soc.*, **134**, 563–582, <https://doi.org/10.1002/qj.235>.
- Wang, Y., and J. Xu, 2010: Energy production, frictional dissipation, and maximum intensity of a numerically simulated tropical cyclone. *J. Atmos. Sci.*, **67**, 97–116, <https://doi.org/10.1175/2009JAS3143.1>.
- , Y. Li, J. Xu, Z. M. Tan, and Y. Lin, 2021: The intensity dependence of tropical cyclone intensification rate in a simplified

- energetically based dynamical system model. *J. Atmos. Sci.*, **78**, 2033–2045, <https://doi.org/10.1175/JAS-D-20-0393.1>.
- Weng, Y., and F. Zhang, 2012: Assimilating airborne Doppler radar observations with an ensemble Kalman filter for convection-permitting hurricane initialization and prediction: Katrina (2005). *Mon. Wea. Rev.*, **140**, 841–859, <https://doi.org/10.1175/2011MWR3602.1>.
- , and —, 2016: Advances in convection-permitting tropical cyclone analysis and prediction through EnKF assimilation of reconnaissance aircraft observations. *J. Meteor. Soc. Japan*, **94**, 345–358, <https://doi.org/10.2151/jmsj.2016-018>.
- Zhang, F., and J. A. Sippel, 2009: Effects of moist convection on hurricane predictability. *J. Atmos. Sci.*, **66**, 1944–1961, <https://doi.org/10.1175/2009JAS2824.1>.
- , and D. Tao, 2013: Effects of vertical wind shear on the predictability of tropical cyclones. *J. Atmos. Sci.*, **70**, 975–983, <https://doi.org/10.1175/JAS-D-12-0133.1>.